FUELS JOINT RESEARCH GROUP

Band 12

Elmar Dohnke

On the high density hydrogen films adsorbed in carbon nanospaces

Editors: Jürgen Krahl, Axel Munack, Peter Eilts, Jürgen Bünger

Cuvillier Verlag Göttingen

On the high density hydrogen films adsorbed in carbon nanospaces

ON THE HIGH DENSITY HYDROGEN FILMS ADSORBED IN CARBON NANOSPACES

A Dissertation

presented to

the Faculty of the Graduate School

at the University of Missouri-Columbia

In Partial Fulfillment

of the Requirements for the Degree

Doctor of Philosophy

---

by

ELMAR DOHNKE

Dr. Peter Pfeifer, Dissertation Supervisor

MAY 2015

Bibliografische Information der Deutschen Nationalbibliothek

Die Deutsche Nationalbibliothek verzeichnet diese Publikation in der Deutschen Nationalbibliografie; detaillierte bibliografische Daten sind im Internet über http://dnb.d-nb.de abrufbar.

1. Aufl. - Göttingen: Cuvillier, 2015

Nonnenstieg 8, 37075 Göttingen

Telefon: 0551-54724-0

Telefax: 0551-54724-21

www.cuvillier.de

1. Auflage, 2015

Gedruckt auf umweltfreundlichem, säurefreiem Papier aus nachhaltiger Forstwirtschaft.

ISBN 978-3-7369-9043-2

eISBN 978-3-7369-8097-6

The undersigned, appointed by the Dean of the Graduate School, have examined the dissertation entitled

ON THE HIGH DENSITY HYDROGEN FILMS ADSORBED IN CARBON NANOSPACES

Presented by Elmar Dohnke,

A candidate for the degree of doctor of philosophy,

And hereby certify that, in their opinion, it is worthy of acceptance.

Professor Peter Pfeifer

Professor Carlos Wexler

Professor Gavin M. King

Professor Bogdan Kuchta

Professor Mark W. Lee

“*See first, think later, then test*”

-W. Sane

ACKNOWLEDGEMENTS

Acknowledgment goes first and foremost to the members of my committee: Drs. Peter Pfeifer, Carlos Wexler, Gavin King, Bogdan Kuchta, Mark Lee, Jürgen Krahl.

I would like to acknowledge all of the people who have contributed to this work and are not mentioned elsewhere:

University of Missouri Physics Graduate Students: Andrew Gillespie Matthew Beckner, Tyler Rash

University of Missouri Physics Undergraduate Students: Sean Sweany, Mark Sweany, Daniel van Hoesen

University of Missouri Physics Research Professor: Dr. Jacob Burress

Drury University Undergraduate Student: Sajan Patra

University of Missouri Biological Engineering Undergraduate Student: Amanda Paige Loelkes

University of Missouri Chemistry Postdoctoral fellow: Dr. Enrico Penk

University of Missouri Physics Machine Shop: Sam Potts, Roderic Schlotzhauer

A special thanks to: Mia Brown and Andrew Gillespie for proofreading this dissertation; Dr. Jacob Burress for his guidance in my first year; my friends here and across the ocean for their moral support, my family for all of their support through the years.

A very special thanks to Dr. Jürgen Krahl and Dr. Peter Pfeifer, for giving me the opportunity to join the University of Missouri Graduate Program.

TABLE OF CONTENTS

LIST OF FIGURES

Figure Page

LIST OF TABLES

Table Page

ABSTRACT

The commercialization of hydrogen-powered fuel cell cars, with their environmentally friendly emissions, provides an opportunity to replace current gasoline powered vehicles. The main drawback of hydrogen as a fuel is the low density at ambient temperatures. The gas needs to be compressed to high pressure or kept under cryogenic temperatures to achieve reasonably long driving ranges. These obstacles can be overcome if the tanks are filled with a porous material that adsorbs a high volume of hydrogen. Many materials are put forward for this purpose, such as metal organic frameworks (MOFs) and engineered carbon nanospaces (synthetic carbon). To get a better understanding of the materials performance, an attempt was made to analyze the properties of the adsorbed hydrogen film. High pressure hydrogen isotherms at cryogenic temperatures (77 K, 50 K) have been studied to estimate adsorbed film properties such as density and thickness. Furthermore, how isosteric heat of adsorption, surface chemistry, and pore size distribution affect the adsorbed film has been investigated. At supercritical temperatures and high pressures, a film density 20% higher than liquid hydrogen at 1 bar and 20 K was obtained. These densities are independent of the isosteric heat of adsorption or pore size distribution. The adsorbed film densities behave similarly for all carbon-based surfaces at 77 K.

Additionally a new method was developed to estimate specific surface areas of gas storage materials from high pressure isotherms and tested against the BET theory. The new method does not require knowledge of the packing fraction or cross-sectional area of an adsorbed molecule in the film. In most cases the new method leads to surface areas comparable to those found using BET theory if cryogenic high pressure isotherms are used.

A new manometric (Sieverts type) adsorption instrument was designed and test, capable of measuring sub- and supercritical hydrogen isotherms at high pressure.

Chapter 1 - Introduction

Over the last decade several attempts were made to decrease the carbon dioxide emissions and dependency on fossil fuels for transportation. Alternative fuels, such as natural gas (Methane) or hydrogen are promising candidates in overcoming some of the issues fossil fuels bring. For example, both fuels can be manufactured from renewable sources. In the case of natural gas, both biomass (biological waste) and carbon dioxide can be converted in synthetic natural gas (SNG) by thermo-chemical processes or by Sabatier reaction, respectively[1]. Hydrogen can also be produced from a renewable source, i.e. water. Water is thereby split into hydrogen and oxygen by electrolysis. Both alternative fuels can be manufactured by using alternative energy sources such as solar panels or wind energy, which increase the overall carbon dioxide efficiency.

One major drawback of the alternative fuels mentioned here is their gaseous state at ambient temperature. For example, 4 kg hydrogen occupies a volume of 45 m^3 at atmospheric pressure and temperature[2]. It makes the usage as an alternative fuel in transportation difficult because large onboard storage capacities are needed. There are three ways to overcome this problem. (i) Liquefaction by cooling the gas to cryogenic temperatures is one approach to increase gas storage capacities. For example, the container ship from TOTE runs on liquefied natural gas which is stored at 111 K[3]. Unfortunately, this method requires heavy cryogenic vessels and a high amount of energy for the liquefaction process, which lowers the total energy efficiency of the system. It is therefore not suited for small transportation vehicles such as cars. (ii) The second one, used by Toyota's first commercial hydrogen fuel cell car, is to store the gas under pressures up to 700 bar. Again, this means heavy, bulky onboard tanks are needed. For example, the carbon-fiber tanks used by Toyota have an outer volume of 122 L and weigh 87.5 kg[4]. Additionally, hydrogen needs to be pressurized to 700 bar at the refueling station, lowering the total energy efficiency of the system. (iii) Another way to overcome the storage obstacle is by

filling the gas tanks with high surface area materials, such as metal organic frameworks (MOFs), activated carbon, or synthetic carbons which densify the gas by adsorbing it at their surface. Therefore these materials reduce the required pressure in tanks without the necessity for cryogenic temperatures, allowing for a smaller, lighter tank design. In physical adsorption, no energy barrier is preventing the molecule from approaching the surface if no diffusional barriers are present. The process does not need activation energy resulting in faster kinetics. Unlike chemisorption, physical adsorption is completely reversible meaning no additional treatment is needed before refiling or during depletion.

Adsorption materials from metal organic frameworks have been proposed as hydrogen storage materials due to their modular surface chemistry[5]. However, they are costly to produce. These materials can only be manufactured in small quantities involving expensive organic linkers and a multi-step synthesis[6]. Compared to metal organic frameworks, chemically activated carbons are generally cheaper to manufacture because they do not involve expensive chemicals. However, their manufacturing process includes multiple steps and the use of corrosive chemicals, such as potassium hydroxide, at high temperatures, and the product must be washed extensively to remove the remaining potassium hydroxide from the surface[7]. Unlike MOFs and activated carbons, synthetic carbons are easy and cheap to make due to a single step manufacturing process, consisting of heating a polyvinyl chloride based plastic under inert gas. The single step process also means it will be easier to mass produce. This plastic type is widely used as food wrap, which could be recycled for making synthetic carbons.

In addition to being easily manufactured, synthetic carbons also possess a range of properties making them favorable for gas storage. Typical high surface area carbons made by chemical activation processes, such as KOH activation, have a broad distribution of pore widths ranging from 0.8 nm to 12 nm, with the majority being between 0.8 nm and 8 nm. Only a small fraction of its pore volume comes from pores smaller than 1 nm (Figure 1). Conversely, synthetic carbons,

made from Saran© (polyvinylidene chloride-co-polyvinyl chloride) or pure polyvinylidene chloride (PVDC), have narrow pore size distributions with the majority of pore widths being smaller than 1 nm. In fact, synthetic carbons have almost 5 times more pore volume from sub-nanometer pores compared with activated carbon (Figure 2). Such narrow pores lead to H_2 adsorption energies as high as 9 kJ/mol, compared to 6 kJ/mol from commercially available activated carbon MSC-30[8]. The enhanced adsorption energy is favorable because it increases the material's capacity for storing hydrogen gas.

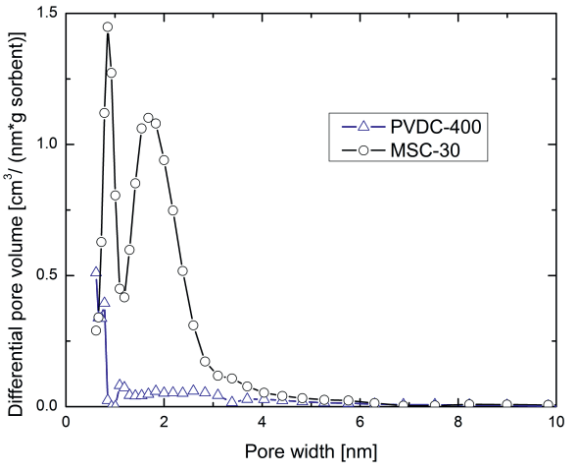

Figure 1 Pore size distribution for PVDC-400 and MSC-30 calculated from quenched solid state functional theory.

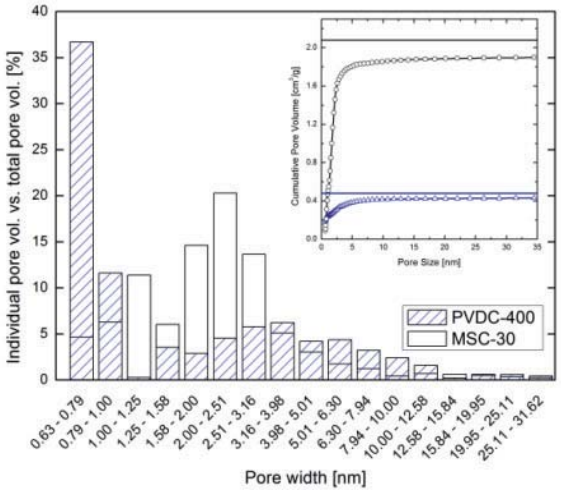

Figure 2 Individual pore volumes and their contribution to the total pore volume.

To improve the materials gas storage capacity it is necessary to understand the mechanisms of gas adsorption in nanoporous materials. We investigate how materials with different pore size distributions and chemical compositions affect the adsorbed hydrogen film under supercritical conditions. Film properties, such as thickness and density, have been estimated by analyzing the high pressure portion of cryogenic isotherms. Additionally, the cross-sectional area of an adsorbed molecule was estimated from the film thickness and specific surface area.

In addition, an attempt was made to estimate the specific surface area from the adsorbed film volume. In contrast to traditional theories such as Brunauer-Emmett-Teller (BET), it neither requires any knowledge about the cross-sectional area of an adsorbed molecule nor makes any assumptions about the packing order of the molecules in the film.

A new high pressure adsorption instrument for cryogenic temperatures was designed to evaluate isotherms at temperatures as low as 7 K and its design and performance has been tested against a commercially available adsorption instrument.

1.1 Principles of Adsorption

Adsorption is defined as the densification of an adsorbate (i.e. gas or liquid) in the vicinity of a bulk interface (adsorbent) and arises from attractive dispersion interaction (van der Waals force, London force), in combination with short range repulsive interactions, between adsorbent and adsorbate. The resulting potential can be described by the Lennard-Jones potential, also referred as 12-6 potential[9]. It is composed of a long range attractive interaction coming from fluctuations in charge distribution of both the adsorbate molecule and surface molecules, and a repulsive component due to overlapping electron orbitals of the gas molecule and substrate at short distance. This type of interaction hinges on the adsorbent properties, such as surface chemistry or geometry, and the nature of the adsorbate.

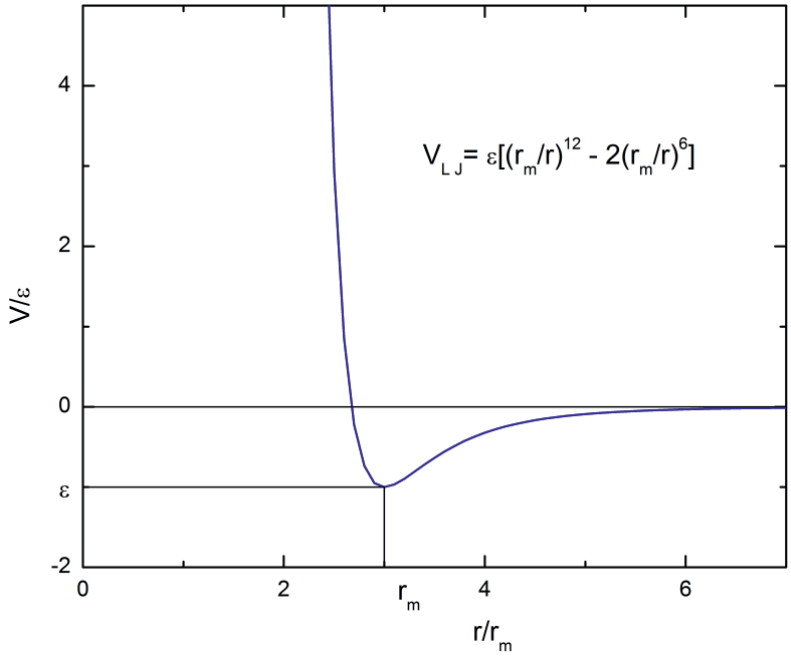

Figure 3 Arbitrary Lennard-Jones potential energy curve as a function of the distance from the sorbent's surface. The minima correspondence to the equilibrium distance between adsorbent and adsorbate.

In narrow pores gas adsorbs strongly due to the overlapping van der Waals potentials coming from both walls and therefore increases adsorption energies. The increase in adsorption energy depends on how much the van der Waals potential overlaps. Molecular dynamics calculations done by J. Burress et al. predict such a behavior. For example, a slit-shaped pore with a 1.3 nm width has calculated maximum adsorption energy of 5.3 kJ/mol on each wall. It also shows a total of two minima, indicating the adsorbed gas forms one layer on each wall. A 0.67 nm width slit-shaped pore shows only one steep minimum with a calculated adsorption energy of 8.1 kJ/mol (Figure 4)[8]. This indicates hydrogen forms only one dense layer in narrow pores but with higher adsorption energy. Everett and Powl show that pore geometry also has an effect on the potential[10]. In slit-shaped pores two walls contribute to the total potential, while cylindrical pores consist of one surrounding wall leading to a much deeper and stretched out potential. For example, the adsorption energy enhancement in a slit pore with twice the width of the adsorbing

molecule is almost zero, but a similarly sized cylindrical pore has a 50% enhancement. This shows adsorption is much stronger in narrow, cylindrical pores and materials with a majority of such pores are therefore favorable hydrogen storage materials.

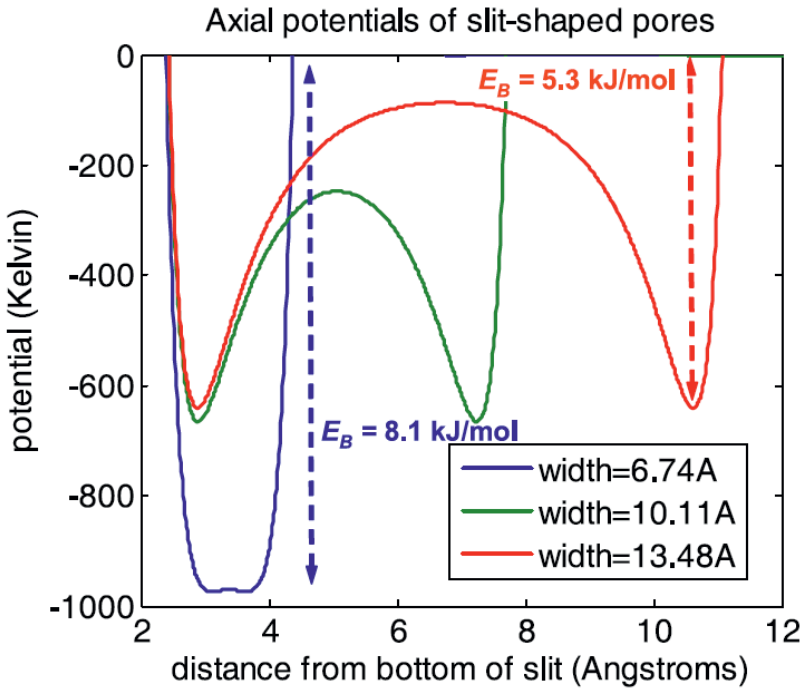

Figure 4 Calculated hydrogen adsorption potential for slit shaped pores of different width.

Although adsorption instruments vary in technique and type, they all measure the same quantity called Gibbs excess adsorption (N_{ex}) and is defined as follows[11].

"The system of interest is a one-component gas in a volume V in the absence and in the presence of an adsorbing surface of area a. In both cases the gas has the same temperature T and pressure p. If N is the average number of molecules in the system with solid present and if N_0 is the average number with solid absent, then the number of adsorbed molecules, by Gibbs' surface excess definition, is $N-N_0$."

The concept can be explained by a simple example sketched in Figure 5.

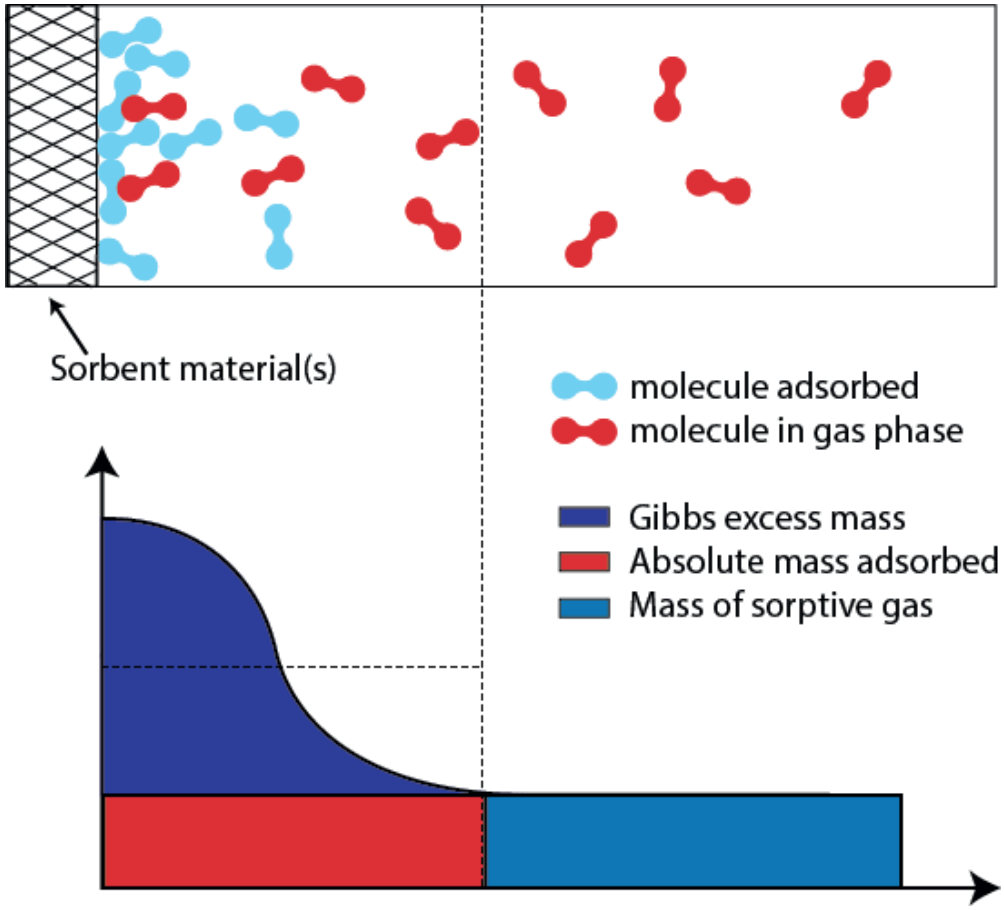

Figure 5 Sorption system in a box of total volume (V) including a certain mass of sorptive gas ($\boldsymbol{m_{system}}$) part of it being adsorbed on the surface of the adsorbent. The adsorbate having the absolute mass ($\boldsymbol{m_a}$) and the Gibbs surface excess mass ($\boldsymbol{m_{g,Gibbs}}$) (after Keller, 2005).

The system consists of a dense, square sorbent material of mass (m_s) and volume (V_s) with only one side exposed to the gas. Thus, the local gas density (ρ) only depends upon coordinate x, directed perpendicular to the plane surface of the adsorbent, and increases towards the surface due to attractive forces from the adsorbent. The boundary between adsorbed gas and non-adsorbed gas is diffuse because molecules from the liquid phase may change their status of being adsorbed or desorbed between two molecular collisions. To overcome this problem, Gibbs proposed a reference system which occupies the same volume as the real system so that:

$$V = V_s + V_a + V_g = V_{s,Gibbs} + V_{g,Gibbs} \quad (1.1.1)$$

Here, subscript a stands for adsorbed layer and g respectively for the gas phase. In the Gibbs picture the concentration of the adsorptive gas remains constant in $V_{g,Gibbs}$ and extents to the adsorbent's surface ($V_{\mathrm{s,Gibbs}} = V_{\mathrm{s}} + V_{\mathrm{a}}$). The mass in the gas phase is therefore given by

$$m_{\mathrm{g,Gibbs}} = \rho_{\mathrm{g}}(V - V_{\mathrm{s,Gibbs}}) \tag{1.1.2}$$

From the mass balance of the adsorptive gas

$$m_{\mathrm{system}} = m_{\mathrm{a,Gibbs}} + m_{\mathrm{g,Gibbs}} \tag{1.1.3}$$

it follows

$$m_{\mathrm{a,Gibbs}} = m_{\mathrm{system}} - m_{\mathrm{g,Gibbs}} \tag{1.1.4}$$

Now consider the same system with the same temperature T and pressure p, but without the attractive force form the adsorbent's surface.

$$m_{\mathrm{system}} = \rho_{\mathrm{g}}^{*}(V - V_{\mathrm{s}}) \tag{1.1.5}$$

Combining 1.1.2, 1.1.4 and 1.1.5 N_{ex} becomes

$$N_{\mathrm{ex}} = \left(\rho_{\mathrm{g}} - \rho_{\mathrm{g}}^{*}\right)(V - V_{\mathrm{s}}) \tag{1.1.6}$$

since $V_{\mathrm{s,Gibbs}}$ is set to V_{s} in Gibbs' approach.

1.2 Microscopic structure of adsorbed film

Most adsorption studies focus on the performance of new adsorption materials in terms of gas storage, meaning how much excess gas can be stored in a system at given pressure and temperature due to the presence of the adsorbent. In particular hydrogen and methane gas are of special interest because they can be used as an alternative fuel in transportation. Only a few groups investigated the microscopic structure of the adsorbed film under supercritical conditions experimentally. For instance, E. Poirier et al. analyzed the density of an adsorbed hydrogen film for different types of MOFs and P. G. Menon did a similar study for nitrogen respectively carbon monoxide on an alumina surface[12,13]. Beyond the adsorbed film density, not much investigation was done in terms of the microscopic structure of the adsorbed film. In the following chapter an effort was made to understand some of the properties of the adsorbed film by analyzing cryogenic isotherms. In particular, the thickness and density of the adsorbed layer is of interest. For example, the film density gives an estimate of how much the gas is “densified” in the presence of the adsorbent and the thickness of the adsorbed layer indicates whether multilayer adsorption occurs. Mainly hydrogen gas as adsorbate is used in this study because of its future as an alternative to fossil fuels in transportation. Furthermore, a variety of adsorbent materials with different properties, such as pore size and chemically altered surfaces are chosen.

Chapter 2 - Linear regime supercritical adsorption isotherm at high pressure

2.1 Theoretical background

Typical gas adsorption instruments only measure a quantity called Gibbs excess adsorption (G_{ex}), or surface excess amount, directly. This quantity describes the amount of gas adsorbed due to the interaction with the adsorbent's surface normalized to the sample mass. A more detailed explanation is given in the introduction. It can be calculated by integrating the adsorbate's density ρ_a over the adsorbed layer's volume V_a, excluding the non-adsorbed gas density ρ_g[14,15].

$$G_{ex} = \frac{N_{ex}}{m_{sample}} = \frac{1}{m_{sample}} \int_{V_{film}} (\rho_a - \rho_g) dV \tag{2.1.1}$$

The common adsorption model assumes that the film reaches saturation at high pressure and does not undergo any phase changes, rearrangements, and behaves like an ideal fluid (incompressible). If this happens, the first term of equation 2.1.1 on the right hand side

$$\int_{V_{film}} \rho_a = N_{film} = \text{const.} \tag{2.1.2}$$

$$N_{ex} = N_{film} - \rho_g V_a \tag{2.1.3}$$

becomes constant, leading to a linear equation. G_{ex} declines as the bulk gas density rises because an increasing amount non-adsorbed gas is removed from the film.

All materials studied in this report exhibit a linear portion in their isotherms at pressures above 20 bar when G_{ex} is plotted versus bulk gas density instead of pressure.

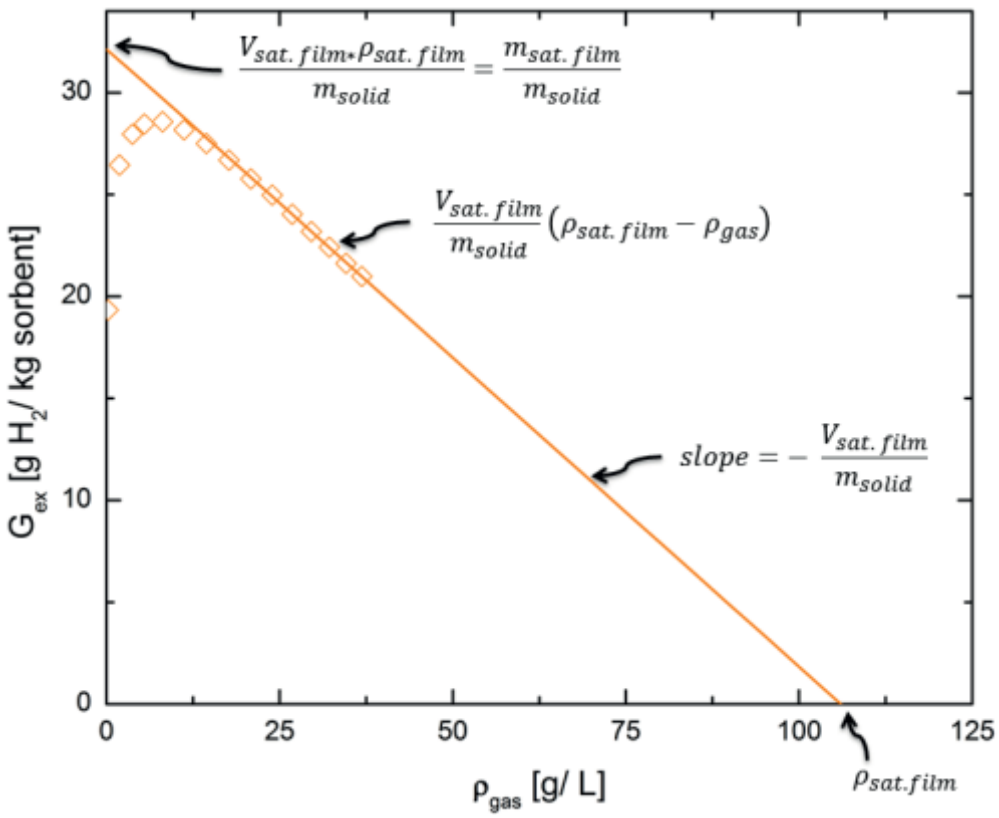

Figure 6 Graph shows the linear fit to excess adsorption at high gas density.

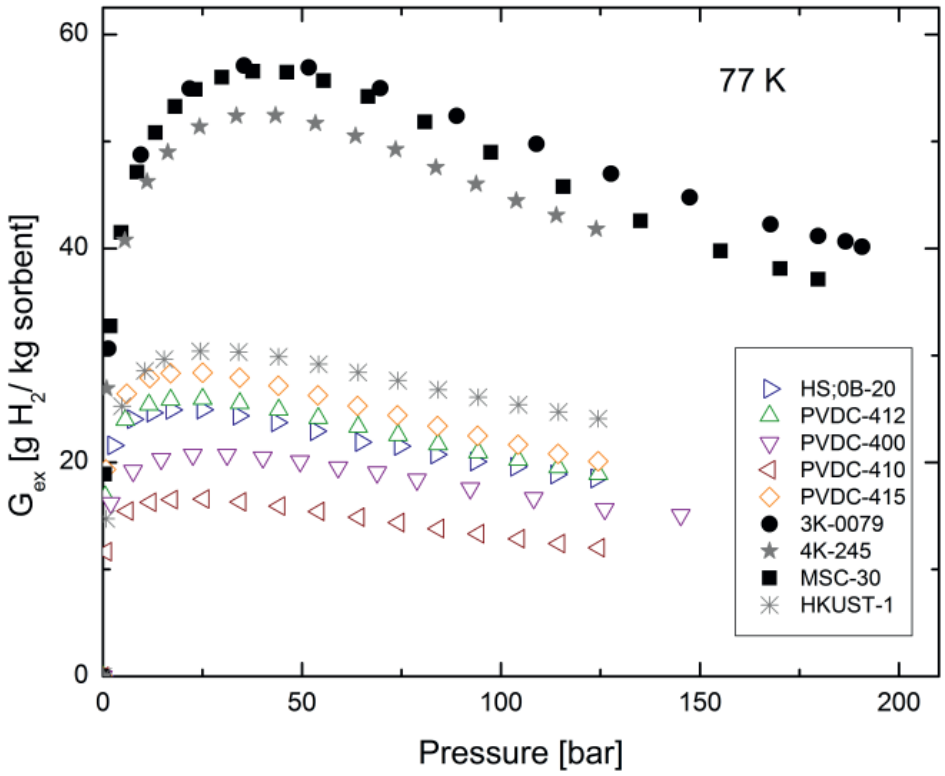

Figure 7 Hydrogen isotherms at 77 K for various adsorbents. Synthetic carbons are represented by colored triangles and diamond, chemical activated carbon are black solid symbols, boron doped chemical activated carbon are grey and MOF grey star

The slope and intercept can be evaluated from a straight line fit to the linear part of the G_{ex} isotherm. Saturated film volume (V_{film}) and monolayer capacity (N_{film}) are represented by slope and intercept, respectively. Furthermore, the saturated film density ($\rho_{sat.\ film}$) can be estimated by extrapolating the linear regime to the abscissa (Figure 6). The intersection represents $\rho_{sat.\ film}$ because at this point excess adsorption (N_{ex}) is zero, meaning the gas density (ρ_g) needs to be equal to the density of the saturated film. This is a novel way to estimate microscopic quantities, such as saturated film density and film thickness from macroscopic values because it does not require any assumption about the size or packed fraction of the adsorbate in its adsorbed state. The adsorbed film thickness is important for the conversion of G_{ex} in absolute adsorption isotherms which are used for isosteric enthalpy of adsorption calculations.

It is worth noting that cryogenic, high pressure isotherms (> 60 bar at 77 K) are needed for this analysis to produce a well pronounced linear regime. An extensive literature search showed that no one has measured supercritical isotherm data which showed the crossing of G_{ex} with the bulk gas density axis.

2.2 Saturated film density estimation $\rho_{\mathbf{sat.\ film}}$

2.2.1 Saturated film density at 77 K (liquid N_2)

Cryogenic hydrogen isotherms at 77 K were collected for different adsorption materials and their saturated film densities evaluated according to the method described earlier. Ultrapure hydrogen gas (99.999% purity) from "Praxair" was used for the experiments. Each adsorption material was heated (200 ^{o}C) under ultrahigh vacuum for four hours to remove moisture or oxygen from the surface. For each sample gravimetric excess adsorption was plotted versus the bulk gas density and the average of multiple sets of experimental points was used for the linear fit. The error was estimated by taking the difference between the maximum and minimum values obtained from all fits of one sample[12]. Furthermore, the linear fit was used to extrapolate G_{ex} which gives an estimation of the saturation film density.

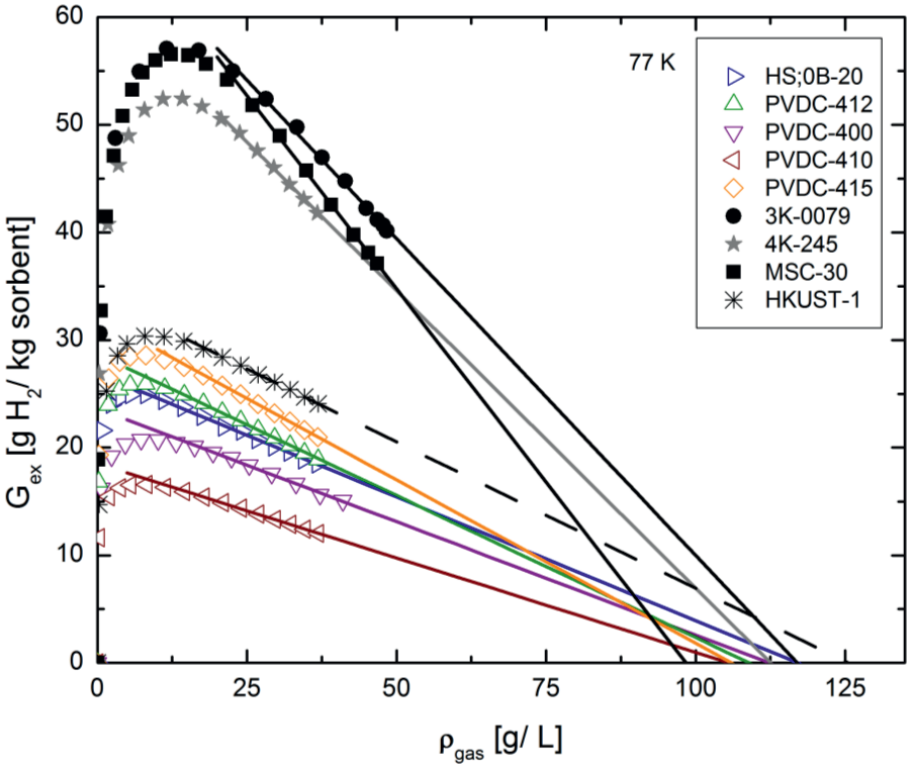

Figure 8 G_{ex} versus bulk gas density at 77 K with the linear portion extended to the x axis. Synthetic carbons are represented by colored triangles and diamond, chemical activated carbons are black solid symbols, boron doped chemical activated carbon shown with grey pentagon and MOF grey star.

Table 1 Calculated saturated H_2 film densities at 77 K from high pressure isotherms

	Sat. film density $\left[\frac{g}{L}\right]$
HS;0B-20	117 ± 7
PVDC-412	106 ± 6
PVDC-400	112 ± 3
PVDC-410	104 ± 5
PVDC-415	106 ± 6
MSC-30	99 ± 5
3K-0079	114 ± 7
4K-245 (3.8 wt% boron)	110 ± 3
HKUST-1	125 ± 7

With the exception of MSC-30 (chemically activated carbon), all material's gravimetric excess isotherms intersect the abscissa above 100 g/L despite their different PSD and surface areas. This density is remarkably high and even surpasses the liquid density of hydrogen (71 g/L) at 20 K.

Sample HS;0B-20 was sent to the National Renewable Energy Laboratory (NREL) for validation, and the isotherm reproduced the one shown here. All of the samples in this study were measured on two different instruments: HTP-1-V-CB, a modified version of the commercially available HTP-1 from Hiden Analytical, and an in-house designed instrument (MU-7K CCHeR), leading to the same result. Thus, it is reasonable to assume instrumental errors are insignificant.

The high densities suggest that the adsorbed hydrogen film has a liquid-like structure above its critical temperature, which is 33 K. A gas above its critical temperature does not condense into a liquid no matter how high the gas pressure is. Thus, it can be concluded that the liquid-like film owes its existence to the adsorption potential present from the material's surface that reduces the spacing between neighboring gas molecules. Such a configuration can happen if the hydrogen molecule becomes trapped by a deep potential well, originating from the material's surface, and loses translational kinetic energy which is transferred to molecules in the gas phase (heat of adsorption). Consequently, this allows the adsorbed molecules to be packed in a dense configuration. Conversely, molecules in the gas phase exhibit strong repulsive interactions (high translational kinetic energy), and therefore cannot be packed in such high densities under normal circumstances.

With the exemption of HKUST-1, most adsorbent surfaces in this study are mainly composed of aromatic carbon hexagons, meaning the adsorption potential is primarily influenced by the van der Waals interaction (London force) between aromatic carbon rings and hydrogen gas. As mentioned in the principle of adsorption chapter, the confinement due to the porous structure also influences the adsorption potential. One could therefore conclude that samples composes primarily of sub-nanometer pores should have higher saturated film densities, as they have a deeper adsorption potential. However, the data shown here do not show a direct correlation between saturated film density and the pore structure. Adsorbents with mainly sub-nanometer pores (synthetic carbons, colored symbols) lead to similar film density as adsorbents

with a variety of pore sizes (chemically activated carbons Figure 8). The data suggest a universal density value for hydrogen (~109 g/L) adsorbed at 77 K on a carbon surface. The only outlier for the carbon-based samples is the commercial activated carbon MSC-30. It has a slightly lower value compared to the rest, possibly due to problems with the linear fitting. MSC-30 has a slight convex bend in the linear regime which makes it more difficult to fit.

The surface of sample 4K-245 was boron-doped after chemical activation to alter the surface chemistry with the goal to create adsorption sites with high binding energy[16–18]. However, the film density is similar to undoped carbon samples, indicating surface deposition of boron atoms does not influence the saturated film density. This is possibly due to the low ratio of boron to carbon atoms on the surface. According to prompt gamma neutron activation analysis (PGAA), this sample has 4 wt.% percent boron, meaning the majority of the surface is composed of carbon atoms, making it similar to undoped chemically activated carbon.

Metal organic frameworks (MOFs), such as HKUST-1, are porous materials made of metal sites connected by organic linkers resulting in a different surface chemistry compared to carbon based samples, and therefore give an indication if there is a correlation between film density and surface chemistry. The MOF HKUST-1 (Sigma-Aldrich, $Cu_3(BTC)_2$) used in this study is composed of copper metal sites and benzene-1,3,5-tricarboxylate as an organic linker. Its pore size distribution consists mainly of 0.7 nm wide pores, comparable to synthetic carbons, and therefore a difference in saturated film density should give an indication whether surface chemistry has an effect on the adsorbed film[19]. The linear interpolation of HKUST-1 gives rise to a saturated film density of 126 g/L, which is 15% higher compared to the average of synthetic carbons (109 g/L), and also the highest value of the materials studied in this report. It seems to suggest surface chemistry can have an influence on the saturated film density. Unfortunately, only one non-carbonaceous

material was available. Additional materials with different surface chemistry would need to be analyzed to verify this result.

2.2.2 Saturated film density at 50 K

For three PVDC based synthetic carbons (PVDC-410, PVDC-412, PVDC-415) and one boron doped activated carbon (4K-245), the saturated film density was estimated at 50 K with the same procedure described earlier.

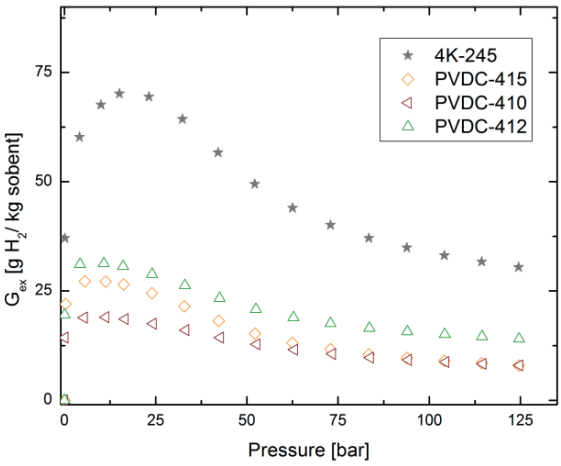

Figure 9 Hydrogen isotherms for various adsorbents at 50 K

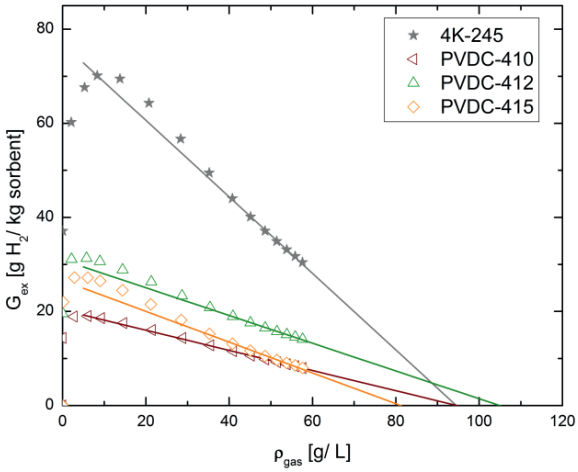

Figure 10 G_{ex} versus bulk gas density at 50 K with the second linear portion fitted. Synthetic carbons are represented by colored symbols and boron doped chemical activated carbon shown with filled grey pentagon.

All isotherms exhibit a maximum in G_{ex} followed by a mostly steep decline until reaching pressures above 60 bar. This behavior is most clearly seen in the activated carbon sample 4K-245. Two pronounced linear regimes with different slopes can be observed if G_{ex} is plotted versus bulk gas density. Because of this circumstance, each linear regime was treated separately, and an average for the entire linear portion was also calculated. Again, the uncertainty was estimated by the spread from the fitted values.

Table 2 Calculated saturated H_2 film densities at 50 K from high pressure isotherms.

	Sat. film density $\left[\frac{g}{L}\right]$ at 50 K		
	Average	1st linear regime	2nd linear regime
4K-245	95 ± 11	85 ± 3	98 ± 5
PVDC-410	95 ± 4	92 ± 3	96 ± 3
PVDC-415	81 ± 11	70 ± 1	85 ± 5
PVDC-412	104 ± 14	90 ± 2	108 ± 8

Interestingly, with the exception of PVDC-412, all average saturated film densities calculated from the entire linear regime at 50 K are below 100 g/L, and therefore lower than the ones obtained from 77 K isotherms. The same is true for the values governed by each individual linear part. This is counter intuitive since one would expect the saturated film density to be higher or equal to the ones calculated from 77 K due to the reduced thermal energy of the gas.

The exceptionally high average saturated film density for PVDC-412 should be taken with caution because the spread of the average fit is 14 g/L, which is rather large and therefore increases the uncertainty.

Published data, for example from Menon or E. Poirier et al., exhibit the same phenomenon for different materials and gases[12,13,20]. For example Menon observed the same behavior for carbon monoxide and nitrogen on an alumina surface[21]. He measured high pressure (3039 bar) N_2 isotherms on Alumina between 273 K and 373 K in increments of 25 K. All adsorbed film densities surpass the liquid N_2 density at its normal boiling point, and the increase in density with temperature is not linear (Graph 11, 12).

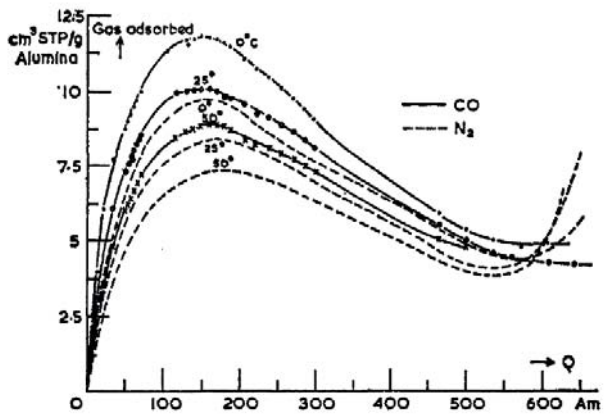

Figure 11 Adsorption isotherms of N_2 and CO on Alumina at high densities (Data from Menon)[12].

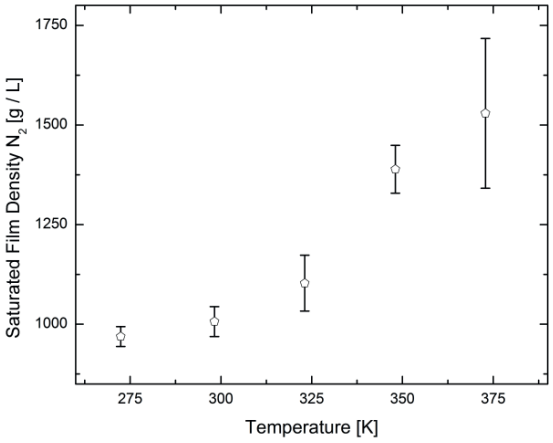

Figure 12 Saturated N_2 film densities on an Alumina surface at different temperatures. The saturated film density increases with temperature

Another example can be found in E. Poirier's hydrogen data on IRMOF-1 (MOF-5; $Zn_4O(C_8H_4O_4)_3$) published in Langmuir 2009[13]. His hydrogen data on IRMOF-1 shows a film density of 62 g/L at temperatures between 50 and 60 K and a rapid increase with increased temperature. From 50 K to 60 K the density changes by 20 g/L, and from 70 K to 77 K, by 25 g/L.

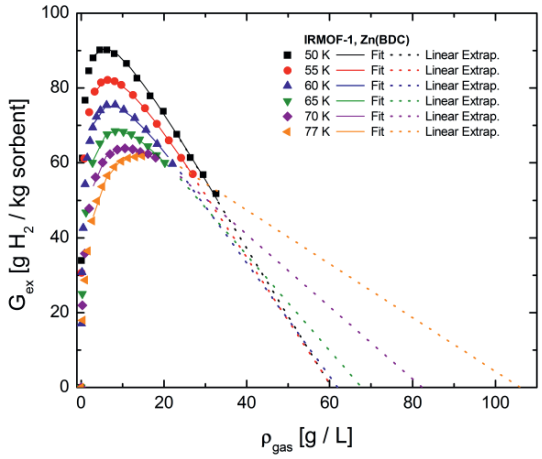

Figure 13 H_2 Adsorption isotherms on MOF IRMOF-1 (MOF-5) as a function of gas density. The graph shows the saturated film density estimated by extrapolating the linear portion to the x axis.

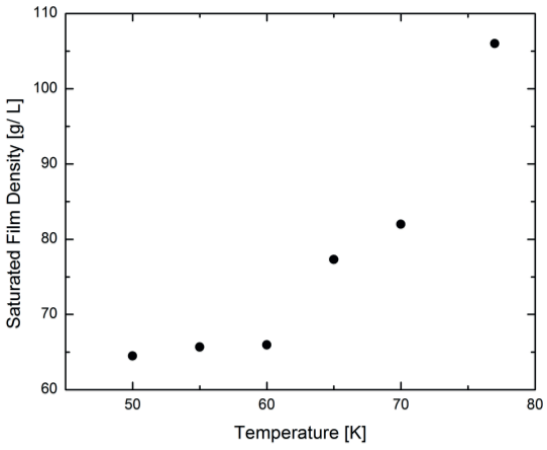

Figure 14 Saturated H_2 film densities from IRMOF-1 as a function of temperature. The saturated film density increases with temperature.

E. Poirier's data seem to suggest that the configuration of the hydrogen film stays constant for temperatures between 50 and 60 K and undergoes changes at temperatures above 60 K. The change in film density is more pronounced with increasing temperatures, indicated by the rapid change from 70 K to 77 K compared to 50 K and 60 K as mentioned above.

The rising saturated film density with increasing temperature suggests that either some of the proposed assumptions (constant film volume, no phase change, or rearrangements) are not valid or that the simple two-phase model does not hold. Another indication for this is the failure of the high pressure adsorption isotherms to reach the abscissa (density axis) as predicted by the model. All 50 K isotherms start to level out at pressures exceeding 60 bar. The phenomenon can be explained if the adsorbed H_2 film exhibits a negative thermal expansion coefficient, such as ice or graphene. This means the adsorbed film decreases in thickness with increasing temperature which can increase its density.

2.3 The influence of heat of adsorption on $\rho_{sat.\ film}$

Gas adsorbing on a surface is an exothermic process (heat is released), and the amount of heat being released is proportional to the interaction between the gas molecule and the surface. Therefore, the change in temperature indicates how strongly the gas is adsorbed. Unfortunately, it is difficult to directly measure the change in temperature during adsorption. It is therefore common to use the isosteric procedure to estimate the interaction energy of the adsorbate-adsorbent system. A description can be found for example in the adsorption book from Rouquerol et al.[22].

For selected samples, the isosteric procedure was used to estimate the heat of adsorption at high surface coverage (1 wt.%). A film thickness of 0.4 nm was used with the BET surface area to convert excess adsorption to absolute adsorption[22]. The choice for high coverage was made because the linear part of the isotherm is at pressures above 20 bar, and therefore the vast majority of the surface was covered with adsorbed molecules. Isosteric heat of adsorption at high coverage was used because the adsorbent's surface is covert with adsorbed molecules similarly to the high pressure part of the isotherm. For at least one sample from each type of material (chemically activated carbon, synthetic carbon, and different surface chemistry) the heat of adsorption was calculated and the uncertainty estimated at 0.5 kJ/mol.

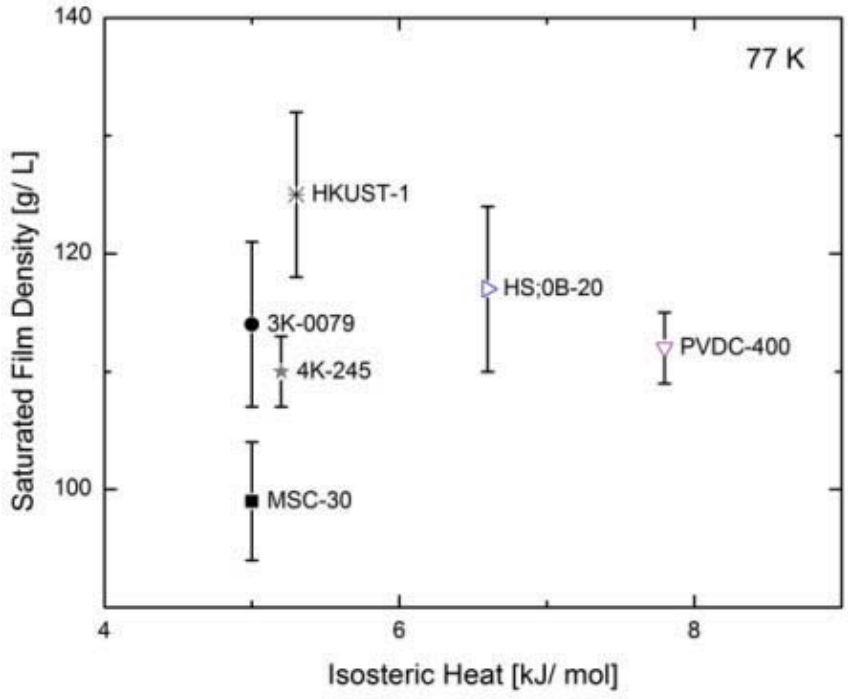

Figure 15 The graph shows the relation between saturated film densities from high pressure H_2 isotherms and the isosteric heat of adsorption, calculated at 1wt.%, for each material

From the heat of adsorption calculations shown in Figure 15, it seems that the heat of adsorption has no influence on the adsorbed film density. For example, material 3K-0079 has a film density comparable to HS;0B-20, but a 1.5 kJ/mol lower adsorption energy. The commercial carbon MSC-30 (chemically activated carbon) shows a different behavior. It has the same heat of adsorption compared to 3K-0079, but its film density is much lower. This is most likely due to the problem with the straight line fit used to calculate the film density of MSC-30, mentioned earlier.

The MOF, HKUST-1, which has the highest film density of all studied samples, has a heat of adsorption value comparable to chemically activated carbon. This strongly supports independence of the saturated film density.

2.4 Intrapore density ρ_{ip}

The previous chapter demonstrated adsorbed hydrogen films can reach densities greater than the liquid state. For most samples such a behavior is only observed at cryogenic temperatures and high pressures, and therefore this method fails at room temperature. One method to obtain information about the gas density inside the porous structure at room temperature is by evaluating the intrapore density ρ_{ip} of the gas. It is defined as the total amount of gas inside the porous network divided by pore volume, and is therefore a weighted average of film density and non-adsorbed gas over the entire sample pore space. The weights are equal to the volume fractions of the pore space that are occupied by the film and gas, respectively. There is no need to make any assumptions about the film thickness or the nature of the pore space.

$$\rho_{\mathrm{ip}}(p,T) = \frac{V_{\mathrm{st}}(p,T)}{\emptyset} \tag{2.4.1}$$

$$V_{\mathrm{st}}(p,T) = G_{\mathrm{ex}}(p,T)(1-\emptyset)\rho_{\mathrm{skel}} \tag{2.4.2}$$

The intrapore density's lower limit is that of the bulk gas, which occurs in systems where a negligible amount of adsorption takes place. Conversely, ρ_{ip} reaches its upper limit if the pores are completely filled with the adsorbed film and an increase of pressure does not introduce more molecules into the pores.

$$\rho_{\mathrm{gas}} \leq \rho_{\mathrm{ip}} \leq \rho_{\mathrm{film}} \tag{2.4.3}$$

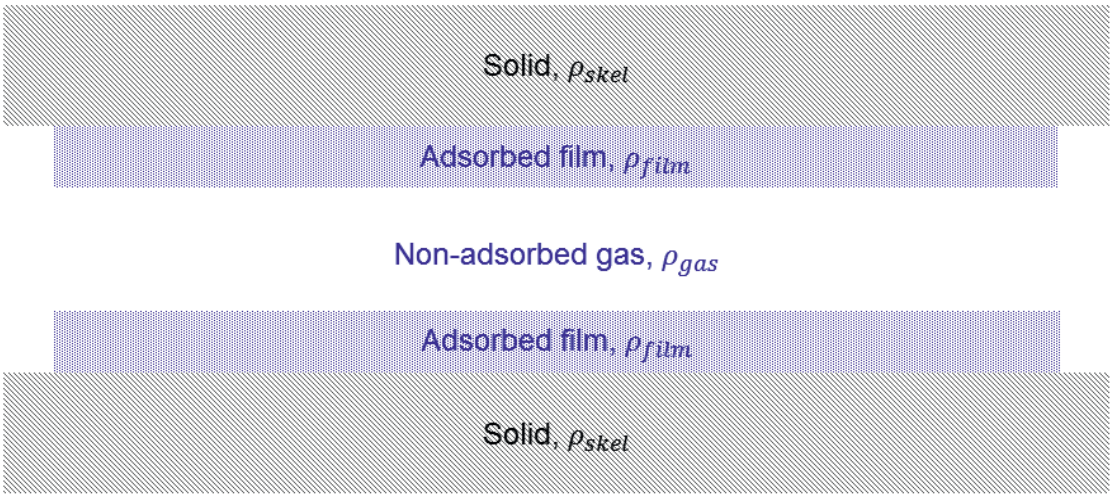

Figure 16 Intrapore density, ρ_{ip}, in a slit shaped pore. Intrapore density ρ_{ip} is represented by the blue area plus non-adsorbed gas.

The significance of ρ_{ip} in the inequality 2.4.3 is that the stored density is easy to determine and is always a lower bound for $\rho_{\mathrm{sat.\ film}}$, which is difficult to measure directly. The film density is of interest because it quantifies by how much the film outperforms non-adsorbed or compressed gas.

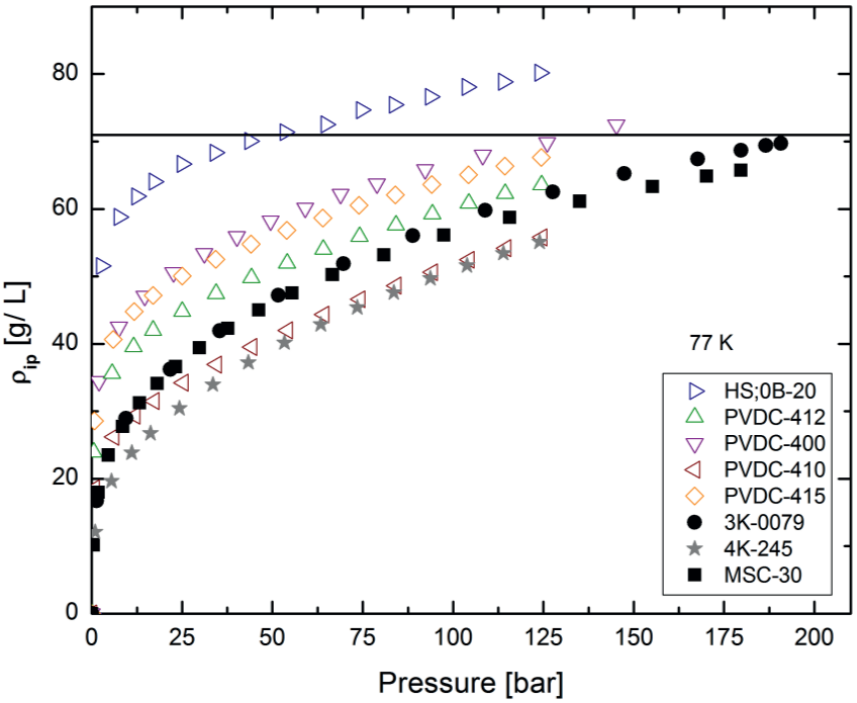

Figure 17 Intrapore density for different adsorbent materials. Synthetic carbons are represented by colored triangles and diamond, chemical activated carbons are black solid symbols, boron doped chemical activated carbon. The horizontal line represent the liquid H_2 density at its normal boiling point and pressure.

The majority of synthetic carbon samples (Figure 17) have high ρ_{ip}, with some even exceeding the liquid density of hydrogen at 20 K (71 g/L). For example HS;0B-20 obtains a ρ_{ip} equal to the liquid density of hydrogen at a pressure of 50 bar which continues to rise with increasing pressure. Chemically activated carbons such as MSC-30 or 3K-0079 also reach a ρ_{ip} of 71 g/L, but require pressures exceeding 200 bar.

This indicates that the actual film density must be even higher, since

$$\rho_{\mathrm{gas}} \leq \rho_{\mathrm{ip}} \leq \rho_{\mathrm{film}} \tag{2.4.3}$$

and therefore indirectly justifies the high saturated film densities governed by the linear extrapolation described earlier because both methods are independent of each other.

Chapter 3 - Saturated film thickness and pore filling factors

3.1 Theoretical background

The saturated film thickness (t_{film}) is a quantity that can be evaluated from the slope of the cryogenic (77 K, 50 K) isotherm's linear regime at high pressures. Knowledge of the adsorbed film thickness is important to convert excess adsorption to absolute adsorption which is used to determine the heat of adsorption with the method of isosteres. It should also give some insight whether the film undergoes changes with temperature and whether supercritical condensation occurs in the pores. The absolute value of the slope represents the volume of the adsorbed film. The thickness of the adsorbed layer is then evaluated by taking the average film volume from each individual fit divided by the material's surface area. The uncertainties are calculated by taking the spread of the obtained values.

$$t_{\mathrm{film}} = \frac{|\mathrm{slope}|}{\mathrm{Surface\ area}} \tag{3.1.1}$$

The surface area was determined from subcritical nitrogen isotherms according to the method described by Brunauer, Emmett, and Teller (BET) using an automated gas-adsorption instrument from Quantachrome (Autosorb-1)[23]. Prior to the adsorption experiment, each material was heated under ultrahigh vacuum for several hours to remove any adsorbed molecules on the surface. With the exception of HKUST-1, each sample's specific surface area was determined in the same pressure range (0.008–0.03 P/P_0) of the nitrogen isotherm. For HKUST-1 a higher pressure range (0.018-0.063 P/P_0) was used to obtain an accurate BET fit.

The amount of pore filling can also be estimated, by taking the ratio of adsorbed film volume and the total pore volume calculated with Gurvitch's rule at a pressure of 0.995 P/P_0 (N_2)[19]. In case of the 50 K measurements, both linear regimes are analyzed separately.

3.2 Saturated film thickness at cryogenic temperatures

Table 3 Adsorbed film thickness estimated from film volume and Bet surface area.

Film thickness calculated with BET surface area [nm]				
	77 K	50 K		
		Average of linear regime	1st linear regime	2nd linear regime
HS;0B-20	0.245 ± 0.02			
PVDC-412	0.245 ± 0.027	0.259 ± 0.07	0.336 ± 0.01	0.243 ± 0.035
PVDC-400	0.268 ± 0.033			
PVDC-410	0.262 ± 0.027	0.317 ± 0.033	0.335 ± 0.014	0.308 ± 0.024
PVDC-415	0.252 ± 0.03	0.276 ± 0.096	0.372 ± 0.093	0.244 ± 0.041
MSC-30	0.255 ± 0.062			
3K-0079	0.234 ± 0.058			
4K-245 (3.8 wt% boron)	0.231 ± 0.035	0.327 ± 0.085	0.402 ± 0.025	0.302 ± 0.038
HKUST-1	0.141 ± 0.015			

Despite the fact that some of the materials have vastly different PSDs and heat of adsorption (1 wt.%), their adsorbed films have similar thicknesses at 77 K. The adsorbed film thickness for all carbon based samples is approximately 0.25 nm and does not show much variation between different sample types. The only exception is the MOF HKUST-1, with a film thickness almost half that of the carbon based samples.

The hydrogen molecule size can be estimated by using the second viral coefficient, which leads to a diameter of 0.29 nm (at 273 K and one bar)[24]. In reality the size should be somewhat smaller because the measurement was performed at 77 K and pressures well above 1 bar. Given the film thickness of 0.25 nm for most of the materials, this corresponds to monolayer adsorption at 77 K.

However, HKUST-1 has a calculated film thickness of approximately half a hydrogen molecule, too small to be physically feasible. This is potentially due to the method used to calculate film thickness. The calculation method assumes that the hydrogen adsorbs onto the same surface area calculated from a subcritical nitrogen isotherm (BET surface area). To estimate a surface area, the BET theory assumes adsorption happens on an energetically homogeneous surface[22].

Infrared spectroscopy and powder neutron diffraction measurements of HKUST-1 reveal at least three distinct binding sites. First hydrogen adsorbs at the Cu sites, then fills the small cage structure near the metal sites before filling the larger pores[25]. This indicates that the gas molecules first form small “islands” of hydrogen around the metal sites and then adsorption happens at lower energy sites.

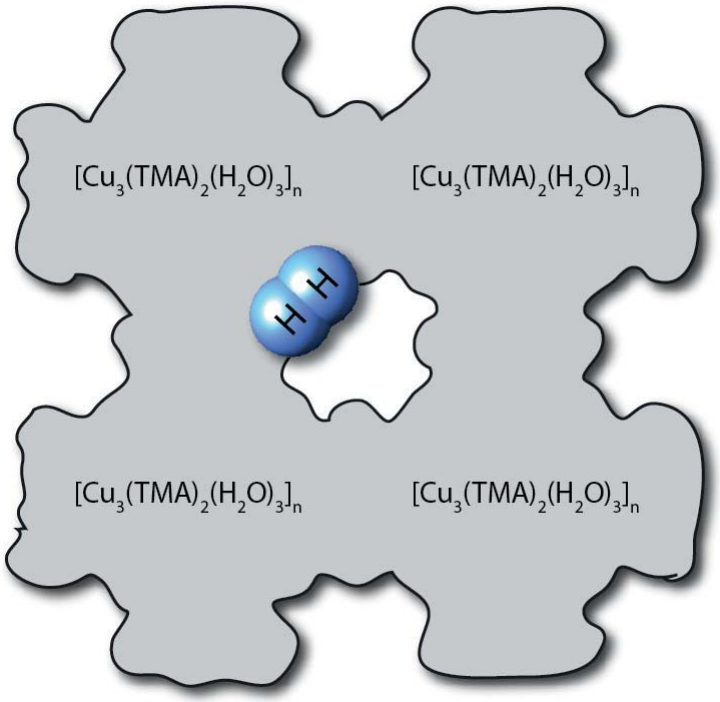

Figure 18 Position of hydrogen after adsorption on HKUST-1

Raman spectroscopy also shows some chemical interaction between Cu and hydrogen (electron donation)[26]. In this case using the BET surface area as a surface reference on which hydrogen adsorbs is not the best choice and most likely leads to misleading results. Thus the monolayer thickness for HKUST-1 calculated with this method should be taken with caution.

For select samples, the average film thickness exhibits a slight increase of 0.04 nm at 50 K compared to calculations done at 77 K. However, this increase is inside the error margin of the calculation, suggesting that either the adsorbed film thickness does not change or if it does, it changes by an amount below the uncertainty at temperatures used here.

This changes if the individual linear regimes from the 50 K isotherms are compared with the ones at 77 K. The adsorbed film thickness, calculated from the first linear regime at 50 K, has the tendency to be on average 0.1 nm thicker than the ones from the higher temperature. Calculating the film thickness from the second linear regime at 50 K yields similar values obtained from 77 K isotherms.

Even though the adsorbed film thickness increases by an average of 0.1 nm if the first linear regime (50 K) is considered; this is not large enough to accommodate 2 layers. An indication for multilayer adsorption would be if the thickness is at least around 0.5 nm, which was not observed for any sample. Thus, there is only monolayer adsorption at 50 K respectively 77 K. This result seems to be independent of the materials pore size (sub-nanometer pores) or surface chemistry.

3.3 Pore filling factors

Table 4 Pore filling factor for different types of adsorbent materials at 77 K and 50 K.

	Pore filling factor [%]			
	77 K	50 K		
		Average of linear regime	1st linear regime	2nd linear regime
HS;0B-20	53			
PVDC-412	40	42	55	44
PVDC-400	44			
PVDC-410	28	33	35	33
PVDC-415	44	48	65	43
MSC-30	34			
3K-0079	34			
4K-245 (3.8 wt% boron)	25	32	44	33
HKUST-1	26			

For activated carbon, the calculated pore filling factors at 77 K show that the adsorbed film occupies between 25% and 34% of the samples pore space. With the exception of HS;0B-20, synthetic carbons (PVDC based) show an increase of 10% compared to activated carbons. HS;0B-20 has the highest pore filling factor of 53%. The average 50 K values are increased between two and seven percent compared to 77 K. The values calculated for the individual linear regimes at 50 K have a trend comparable to the saturated film thickness. The first linear regime gives rise to increased pore filling factors while the second linear regime yields pore filling factors comparable to the high temperature values.

These values show that the adsorbed gas occupies, on average, 30% of the total pore space for activated carbons respectively 44% for synthetic carbons. Changing the temperature does not seem to have an impact on the average (entire linear regime) pore filling. However if the individual linear regimes from the low temperature isotherms are used for comparison, then the pore filling shows an increase at lower temperature. With an increase of 7% sample PVDC-410 has the lowest increase of all measured materials and PVDC-415 with 21% being the highest one.

The comparison between the second part of the linear regime and the values calculated from 77 K leads to similar pore fillings factors. The calculations done on the individual linear regimes should be taken with caution because not many data points could be used for the analysis. This is especially true for the first part of the linear regime due to the small pressure range it occurs. Activated carbon samples saturate at higher pressures compared to synthetic carbons and therefore have less data points in the linear part of the isotherm, which makes the calculations less accurate.

Nevertheless, none of the calculated pore filling factors are high enough to support capillary condensation. Capillary condensation would be indicated by filling factors above 90%, since the adsorbed film would occupy almost the entire pore space. Even materials with sub-nanometer pores do not show any capillary condensation at temperatures as low as 50 K.

Based on the results shown, it is incorrect to use the total pore volume of the sample to convert excess adsorption to absolute adsorption, as commonly used in literature[27].

3.4 Saturated film thickness based on the saturated film density $\rho_{\text{sat. film}}$

The film thickness can also be directly calculated from the saturated film without the knowledge of the surface area or any assumption of the packing fraction. For conventional reasons film thicknesses calculated from $\rho_{\text{sat. film}}$ are labeled as $t_{\text{film }\rho}$.

Consider a slab of adsorbed, liquid like, H_2 with a number density $N_{\text{liq.}}$ (number of molecules per volume) and decompose it into layers of thickness equal to the monolayer thickness t_0. The decomposition of the multilayer slab into monolayers can be done by using the adsorbed molecules footprint σ and the basal area A.

$$N_{\text{liq.}} = \frac{\text{number of molecules in slab}}{\text{volume of slab}} \tag{3.4.1}$$

$$N_{\text{liq.}} = \frac{\text{number of monolayer in slab} * \text{number of molecules in monolyer}}{\text{number of monolayers in slab} * \text{volume of monolayer}} \tag{3.4.2}$$

$$N_{\text{liq.}} = \frac{\text{number of molecules in monolayer}}{\text{volume of monolayer}} \tag{3.4.3}$$

$$N_{\text{liq.}} = \frac{\frac{A}{\sigma}}{A * t_0} = \frac{1}{\sigma * t_0} \tag{3.4.4}$$

In the case of an isotropic molecule equation 3.4.4 simplifies and the film thickness can be calculated.

$$N_{\text{liq.}} = \frac{1}{{t_0}^3} \tag{3.4.5}$$

$$t_{\text{film }\rho} = t_0 = \left(\frac{\rho_{\text{sat. film}} * \text{N}_\text{A}}{M}\right)^{-\frac{1}{3}} \tag{3.4.6}$$

For the decomposition of the slab into monolayers, it is important that the film is saturated and the adsorbed H_2 density stays constant throughout the slab.

Table 5 Film thickness calculated from saturated H_2 film density, assuming an isotropic adsorbate molecule.

	Film thickness calculated from $\rho_{\text{sat. film}}$ [nm]			
	77 K		50 K	
		Average of linear regime	1st	2nd
HS;0B-20	0.306 ± 0.006			
PVDC-412	0.317 ± 0.011	0.317 ± 0.015	0.334 ± 0.002	0.314 ± 0.007
PVDC-400	0.310 ± 0.009			
PVDC-410	0.317 ± 0.008	0.328 ± 0.005	0.331 ± 0.003	0.327 ± 0.003
PVDC-415	0.315 ± 0.009	0.345 ± 0.015	0.363 ± 0.001	0.34 ± 0.006
MSC-30	0.323 ± 0.018			
3K-0079	0.310 ± 0.007			
4K-245 (3.8 wt% boron)	0.310 ± 0.012	0.328 ± 0.13	0.34 ± 0.004	0.324 ± 0.006
HKUST-1	0.3 ± 0.008			

Interestingly, at 77 K the film thickness calculated from saturated film density is on average 0.06 nm thicker compared to the ones calculated with the BET surface area and film volume. One explanation is the different size in probing molecules. BET surface areas are based on subcritical nitrogen adsorption isotherms but the film volume comes from supercritical hydrogen isotherms. The hydrogen molecule is smaller compared to nitrogen and therefore can excess a wider pore space. This effect dominates in materials with extreme narrow pores. The materials used for this study are manly composed of pores larger than 0.6 nm which can be seen from the cumulative pore volume graph shown in the introduction. The cumulative pore volume reaches the same volume measured from subcritical nitrogen isotherms at 0.995 P/P_0 (N_2) and therefore is a good representation about the total pore space of each sample.

Nevertheless, this increase does not change the assumptions made earlier. The film consists of a monoatomic layer and shows very little variation between different materials. Even HKUST-1 exhibits a H_2 film thickness comparable to the rest of the measured materials, supporting the conclusions made earlier about the validity of the BET surface area for this MOF.

Chapter 4 - Adsorbed molecule footprint

4.1 Theory

The footprint area of an adsorbed H_2 molecule is another quantity which can be obtained from analyzing the linear part (> 20 bar) of the isotherm.

The saturated film density ($\rho_{\text{sat.film}}$) needs to be converted to the number density ($N_{\text{sat. film}}$), meaning the number of molecules in the adsorbed monolayer divided by the monolayer volume.

$$N_{\text{sat.film}} \equiv \frac{\text{number of molecules in monolayer}}{\text{volume of monolayer}} = \frac{N}{N * h * \alpha} \tag{4.1.1}$$

This equation can be simplified if the H_2 molecule is treated as isotropic. The monolayer thickness h can then be expressed by equation 4.1.2.

$$h = \frac{1}{\sqrt[3]{N_{\text{sat.film}}}} \tag{4.1.2}$$

$$N_{sat.film} \equiv \frac{number\ of\ molecules\ in\ monolayer}{volume\ of\ monolayer} = \frac{1}{\alpha * \frac{1}{\sqrt[3]{N_{\text{sat.film}}}}} \tag{4.1.3}$$

$$\alpha = (N_{\text{sat.film}})^{-\frac{2}{3}} = \left(\frac{\rho_{\text{sat.film}} * \mathrm{N_A}}{M_{\mathrm{H_2}}}\right)^{-\frac{2}{3}} \tag{4.1.4}$$

with $M_{\mathrm{H_2}} = \text{Molar mass of hydrogen};\ \mathrm{N_A} = \text{Avogadro's number}$

It is worth noting that the method described here uses only the assumption that an adsorbed hydrogen molecules is isotropic and the film forms a monolayer, which are widely used for supercritical adsorbed hydrogen in literature[15]. Furthermore, no knowledge about the packing of the adsorbed molecules is required and the method is independent of the type of gas used for the isotherms. For non-isotropic molecules equation 4.1.4 is still useful if the thickness of the

adsorbed monolayer is known or estimated from the film volume and the BET surface area as described earlier.

4.2 Cross-sectional area of an adsorbed molecule at 77 K

The same materials and cryogenic H_2 isotherms shown in prior chapters are used to calculate adsorbed H_2 footprint and the uncertainty was estimated from the theory of error propagation, assuming the absolute uncertainty in saturated film density to be the spread of the individual fits.

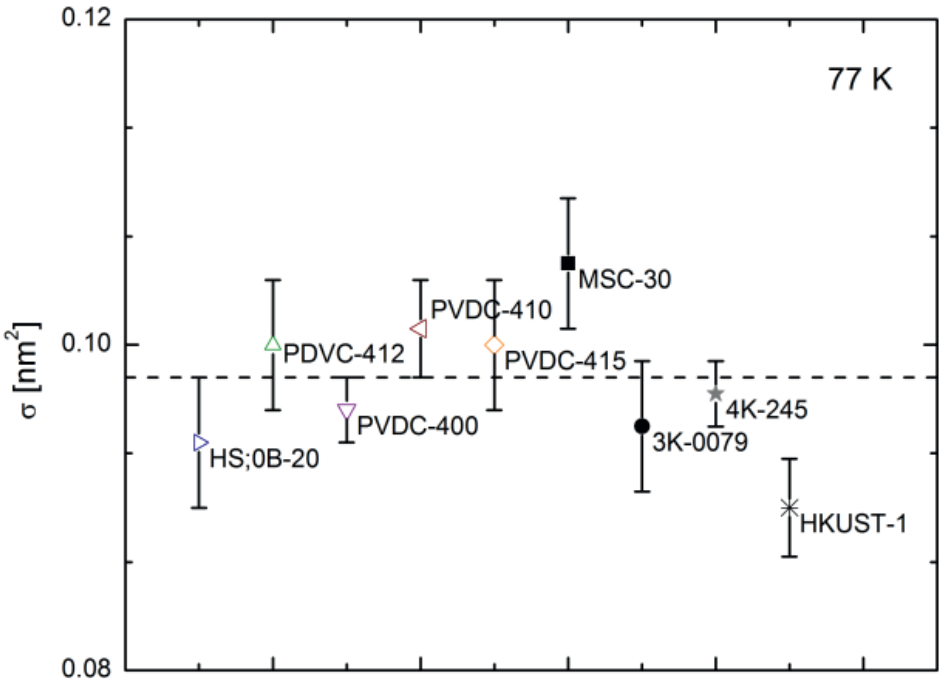

Figure 19 Cross-sectional area of an adsorbed hydrogen molecule at 77K. Synthetic carbons are represented by colored triangles and diamond, chemical activated carbons are black solid symbols, boron doped chemical activated carbon. The average is represented by the dotted line.

Table 6 Cross-sectional area of an adsorbed hydrogen molecule at 77 K and 50 K for a variety of adsorbent materials.

	α [nm^2]	
	77 K	50 K (average)
HS;0B-20	0.094 ± 0.004	
PVDC-412	0.100 ± 0.004	0.101 ± 0.009
PVDC-400	0.097 ± 0.002	
PVDC-410	0.101 ± 0.003	0.108 ± 0.003
PVDC-415	0.100 ± 0.004	0.119 ± 0.010
MSC-30	0.105 ± 0.004	
3K-0079	0.095 ± 0.004	
4K-245	0.097 ± 0.002	0.108 ± 0.008
HKUST-1	0.090 ± 0.003	

At 77 K the average area occupied by an adsorbed H_2 molecule is between 0.09 ± 0.003 nm^2 for MOF HKUST-1 and 0.105 ± 0.004 nm^2 for the commercially available activated (KOH activated) carbon MSC-30. With the exception of MSC-30 most synthetic and chemical activated carbons exhibit, with little variations, values around 0.098 nm^2. The variations are within the uncertainty margins and therefore must be considered as not significant.

The exceptional high value for MSC-30 should be taken with care, due to difficulties with the linear fit used to estimate the saturated film density $\rho_{\mathrm{sat.film}}$. As described in the linear regime chapter, MSC-30 exhibits a slight convex bend in the linear regime, making the fit more difficult. This circumstance can lead to a higher footprint area for the adsorbed molecule.

The calculated adsorbed H_2 footprint for MOF HKUST-1 is 0.09 ± 0.003 nm^2, the lowest footprint of all studied materials and 0.008 nm^2 smaller compared to the average 0.098 nm^2 (excluding MSC-30, HKUST-1). The difference is two times larger as the average uncertainty

($0.004\ nm^2$) of the measurements, suggesting the adsorbed molecules footprint is influenced by the surface of the adsorbent. A study on various adsorbed molecule cross sections conducted by A. L. McClellan found similar results. They concluded that the size of the adsorbed molecule is not constant, but can vary with the adsorbent[28].

Further studies on materials with different surface chemistry, i.e. MOFs, need to be conducted to make a definite conclusion if the surface chemistry has an influence on the molecule's footprint.

Furthermore, the heat of adsorption at high coverage (1wt.%) have been calculated with the isosteric method mentioned earlier and compared to the footprint governed at 77 K. Samples exhibiting high heat of adsorption such as PVDC-400 or HS;0B-20 don't show different footprints compared to materials of lower heat of adsorption. For example chemical activated 4K-245 has 5.2 kJ/mol, which is 2.6 kJ/mol lower as the synthetic carbon PVDC-400, but both have similar adsorbed H_2 cross section areas, indicating the heat of adsorption does not influence the adsorbed molecule footprint. The same can also be found for sample HS;0B-20 and 3K-0079.

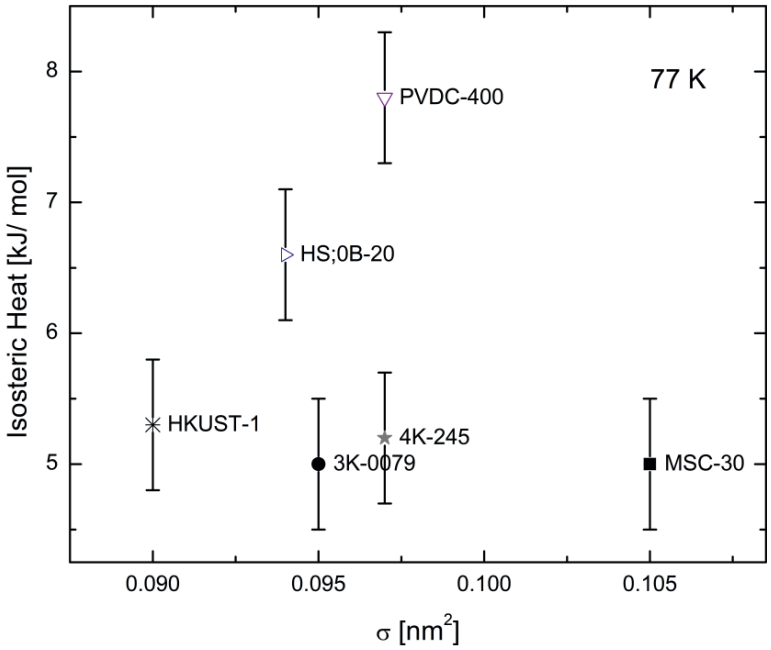

Figure 20 Isosteric heat of adsorption and its influence on the cross-sectional area of an adsorbed molecule.

4.3 Cross-sectional area of an adsorbed molecule at 50 K

The cross section of an adsorbed H_2 molecule, calculated from the average saturated film density at 50 K, show a slight increase for most adsorbents used in this study.

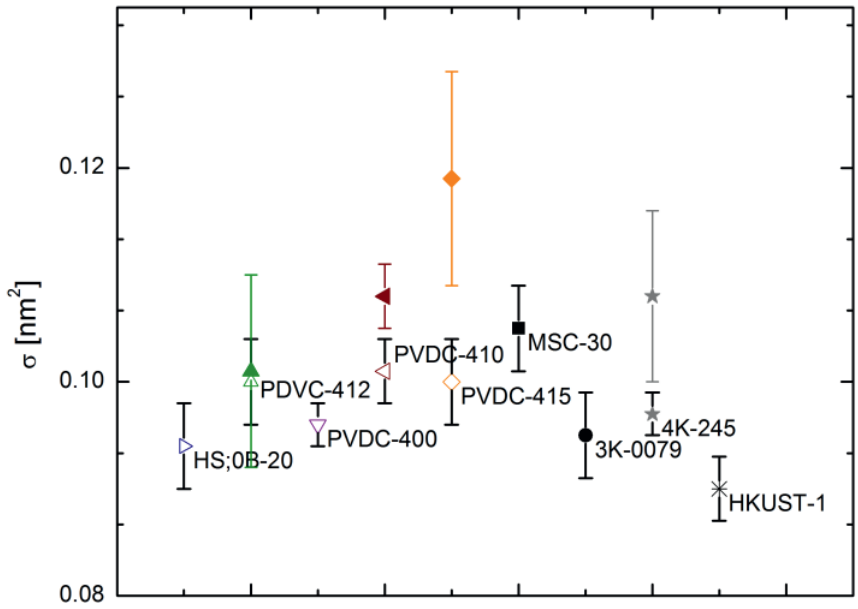

.

Figure 21 Molecular cross-sectional area from average saturated film density at 50 K respectively 77 K. Unlabeled symbols represent 50 K values

The same observation is made for the molecule footprint areas calculated from individual linear regimes at 50 K independent if the first or second part of the linear regime is used. Interestingly, cross sections areas evaluated from the first and second part of the linear regime are comparable. It seems that adsorbed H_2 molecules occupy less space at 77 K compared to 50 K.

Table 7 Cross-sectional areas of adsorbed H_2 at 50 K calculated from individual linear portions

	α [nm^2] at 50 K	
	1st linear regime	2nd linear regime
PVDC-412	0.112 ± 0.002	0.098 ± 0.005
PVDC-410	0.110 ± 0.002	0.107 ± 0.002
PVDC-415	0.132 ± 0.001	0.116 ± 0.005
4K-245 (3.8 wt% boron)	0.116 ± 0.003	0.105 ± 0.004

One explanation for this phenomenon can be made by assuming the hydrogen is oriented in different ways on the surface. By assuming the hydrogen molecule has a dumbbell shape, the molecule can be adsorbed in two configurations on the surface. One configuration is by lying on the surface and the second one is perpendicular to it and therefore takes less space on the surface.

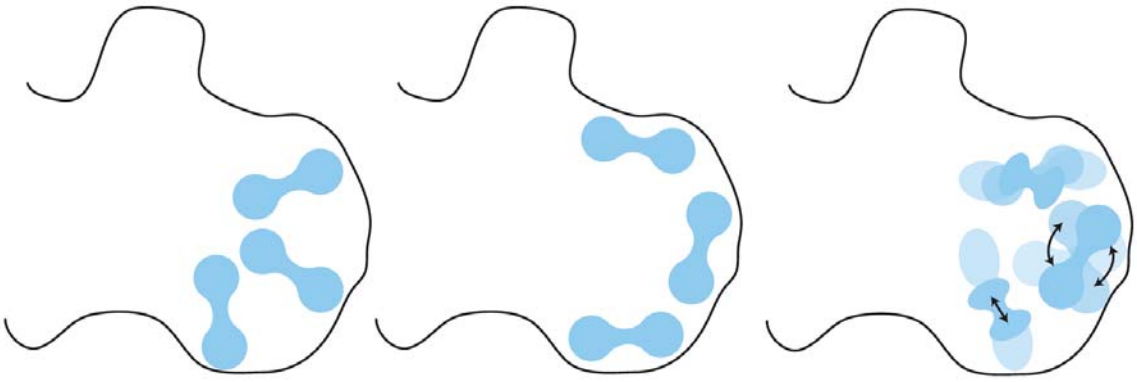

Figure 22 Schematic orientation of H_2 molecule adsorbed in pore

From the calculated cross section areas it seems that the adsorbed hydrogen at 77 K is in the perpendicular configuration due to the smaller footprint and at 50 K lying flat on the surface.

If this explanation is correct then the assumption of hydrogen being an isotropic molecule is no longer valid and therefore the film thickness needs to be taken into consideration for accurate molecule footprint estimation.

The adsorbed cross section areas for non-isotropic H_2 molecule are calculated with the help of the film thickness calculated in chapter 2. On average an increase of 35% compared to the isotropic case can be found. At this moment it is not clear which of the calculations lead to the physical correct value.

Chapter 5 - Surface area determination

5.1 Overview and theory of commonly used techniques

The determination of specific surface areas of porous materials is one of the single most important metric, when it comes to a materials gas storage performance. Surface area measurements are not only used for screening new material's performance with regards to gas storage or separation, it is also used to test electrodes in fuel-cell applications and batteries. Typically, subcritical nitrogen isotherms are collected and the specific surface area estimated with the Brunauer-Emmett-Teller (BET) theory.

Exceptionally high specific surface areas of 6000 m^2/g to 8000 m^2/g have been reported but are controversial; i.e. M. Dresselhaus reports a specific surface area of 3606 m^2/g for KOH activated, PVDC-based carbon[29]. By comparison, a single graphene sheet has 2630 m^2/g, 38% smaller than the reported value[30]. The difference cannot entirely be attributed to additional surface area from edges because the sample is mainly composed of solid material according to scanning electron microscopy pictures. In controversial cases, such as MOFs, researchers found different specific surface areas for the same experimental subcritical N_2 isotherm analyzed with the BET theory or the method described by Langmuir. Using multiple adsorbates of same size such as argon, nitrogen, or oxygen does not give better consistency.

So why is it difficult to measure specific surface areas of porous materials? Typically one needs to form a monolayer of the adsorbate and count how many there are in one layer (n_{mono}) and multiply it with the cross-sectional area (α) of the probing molecule. The specific surface area $\sum$ (surface area per gram of material) is then given by equation 5.1.1.

$$\sum = \frac{n_{\mathrm{mono}} * \alpha}{m_{\mathrm{solid}}} \tag{5.1.1}$$

Both BET and Langmuir theory are based on this concept, and they differ only in how the monolayer capacity is evaluated. Usually subcritical adsorption data at low pressure (sub-monolayer coverage) are analyzed and compared to theoretical adsorption models, such as BET theory or Langmuir theory. Both models mentioned here use n_{mono} and the adsorption strength, c, as parameters. The monolayer capacity n_{mono} is then obtained by fitting the theoretical isotherm to the experimental data. Next, $\sum$ can be calculated by converting n_{mono} to the number of adsorbed molecules and multiplying it with the cross-sectional area of the probing molecule. Typically 0.162 nm^2 is used for nitrogen gas. The Langmuir theory will not be discussed here due to the common usage of the BET theory.

Multiple problems can occur with this methodology. In subcritical adsorption, i.e. N_2 at 77 K or Ar at 87 K, there is no film configuration that corresponds to a single layer. Normally multiple configurations can coexist as islands. For example, in some areas a monolayer can form but other areas are not "wetted" by the adsorbate. Materials with energetically inhomogeneous surfaces, such as MOFs, are particularly strong candidates for this phenomenon. At pressures approaching the coexistence pressure of bulk liquid and gas, usually ~1 bar if the experiment is carried out at the boiling point of the adsorbate, most surface sites are covered with multilayers and capillary condensation can occur.

Another difficulty arises from the fits themselves. There is no unique way to fit a particular model to the experimental data. Different models can be equally well fit to a given set of experimental isotherms, but n_{mono} is not equal. For example the monolayer capacity calculated with the BET theory is not equal to the monolayer capacity calculated with the Langmuir theory.

$$n_{\text{mono, BET}}(P_1, P_2) \neq n_{\text{mono, Langmuir}}(P_1, P_2) \tag{5.1.2}$$

Using only one model does not solve the problems. Within a fixed model, different pressure intervals can lead to equally good fits of the experimental data for the chosen pressure range, but lead to different n_{mono} values.

$$n_{\text{mono, BET}}(P_1, P_2) \neq n_{\text{mono, BET}}(P_1, P_2) \tag{5.1.3}$$

The subcritical nitrogen isotherm for a KOH activated synthetic carbon was recorded on an automated gas-adsorption instrument from Quantachrome (Autosorb-1), and the specific surface area determined at different pressure intervals. Depending which pressure range was used, the specific surface area ranged from 2660 m^2/g to 3470 m^2/g. It is therefore important to report the pressure interval used to fit the theoretical BET isotherm. Unfortunately not many publications indicate this range, which leads to difficulties comparing materials or measurements.

Table 8 Specific surface area calculated from BET theory for different pressure intervals.

Pressure interval $\left[\frac{P}{P_0}\right]$*	Points	Specific surface area $\left[\frac{\text{m}^2}{\text{g}}\right]$	C value	R^2
0.008-0.03	7	2660	512	0.99977
0.03-0.15	7	3330	79	0.999279
0.04-0.24	7	3470	57	0.999886

*P_0= saturation pressure at normal boiling point

To minimize the subjectivity in the assessment of the pressure interval, Rouquerol mention three criteria which should be satisfied to get a reliable surface area measurement with BET theory[22].

1. The obtained c value needs to be positive since it is related to the heat of adsorption. A more detailed description can be found in the adsorption book from Rouquerol[22].

2. The pressure range is limited to the interval in which $n(1 - P/P_o)$ continuously increases with P/P_0.
3. The calculated pressure from $1/(\sqrt{C} + 1) = (P/P_0)_{N_{\text{mono}}}$ should not differ more than 10% from the one corresponding from the BET fit.

All Pressure intervals are compliant with criteria one and two. The first pressure range (0.008-0.03 P/P_0) is typically used for microporous materials, but in this case fails to fulfill the third criteria because N_{mono} from the BET fit is 13% lower.

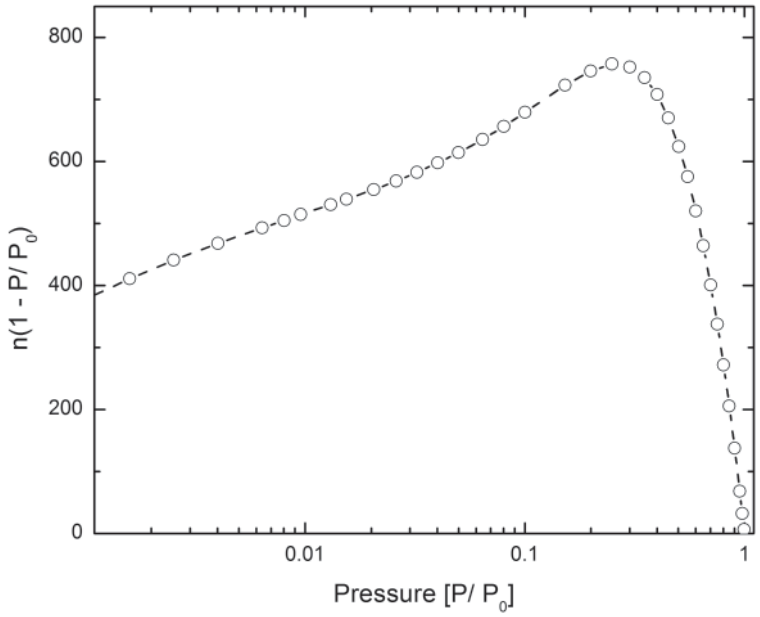

Figure 23 Graph of $n(1 - P/P_o)$ versus pressure (second criteria of Rouquerol). The applicable pressure interval for the BET fit needs to be below $P/P_0 < 0.2$.

Nevertheless, it does not give a unique specific surface area because there are two valid pressure intervals remaining, meaning the specific surface area can be either 3330 m^2/g or 3470 m^2/g.

An additional problem lies in the cross-sectional area α used to obtain specific surface areas with BET. Usually a fixed standard such as 0.167 nm^2 for N_2 at 77 K is used. This value

originates from assuming the packing of N_2 in the monolayer to be identical to the packing in its liquid state[23]. Extensive studies by McClellan and Harnsberger indicate the molecule's α is not a constant, especially for porous materials; the variation can be as much as 21%[28]. For example nitrogen, one of the most common gases used for BET theory, can have a cross-sectional area reaching from 0.13 nm^2 to 0.20 nm^2, depending on the surface of the adsorbent and temperature. Cascarini de Torre et al. has conducted simulations of various gases on amorphous carbon and calculated α at different temperatures. There was a large variation in adsorbate cross-sectional areas near the point where the number of adsorbed molecules reaches the monolayer capacity. This pressure range is usually picked to determine the BET monolayer capacity making the determination of α nontrivial[31]. Furthermore, confinement due to pores and surface geometry, such as highly curved areas and binding sites with variable binding energies, can also influence α. Thus, α should be treated as an experimental quantity not as a universal constant, leading to the problem of how to determine α easily.

In most cases nitrogen gas is used to obtain specific surface areas, but the material under investigation is designed for a different adsorbent, such as hydrogen or methane. In this case the surface seen by nitrogen can differ from the surface seen by hydrogen or methane. This is especially true for hydrogen because its size is significantly smaller than N_2 (half the size of N_2) and may access additional adsorption sites. Therefore the same "yardstick" should be used, meaning the specific surface area should be evaluated with the same molecule under investigation.

5.2 Surface area determination from the saturated film density

The specific surface area $\sum$ is defined as the surface area normalized to the mass of the material, as mentioned in the introduction of this chapter. It can also be expressed in terms of the volume and thickness of the adsorbed film by equation 5.2.1

$$\sum_{\text{sat. film}} = \frac{V_{\text{sat. film}}}{t_{\text{sat. film}} * m_{\text{solid}}} \tag{5.2.1}$$

As described in an earlier chapter, supercritical excess adsorption isotherms at cryogenic temperatures exhibit a maximum and become linear afterwards. The saturated film volume $V_{\text{sat. film}}$ and thickness $t_{\text{sat. film}}$ can be obtained from the saturated film density $\rho_{\text{sat. film}}$ by the method described in the earlier chapter.

$$t_{\text{sat. film}} = \left(\frac{\rho_{\text{sat. film}} * \mathrm{N_A}}{\mathrm{M}}\right)^{-\frac{1}{3}} \tag{5.2.2}$$

$$V_{\text{sat. film}} = -\text{slope} \tag{5.2.3}$$

By combining equation 5.2.1, 5.2.1 and 5.2.3, $\sum$ can be calculated according to

$$\sum_{\text{sat. film}} = \frac{-\text{slope}}{m_{\text{solid}}} \left(\frac{\rho_{\text{sat. film}} \mathrm{N_A}}{\mathrm{M}}\right)^{\frac{1}{3}} \tag{5.2.4}$$

where M is the molar mass of the used gas and $\mathrm{N_A}$ is the Avogadro's constant.

Equation 5.2.4 based on the assumptions that the film

1. behaves like an incompressible fluid (ideal fluid).
2. reached saturation at sufficient high pressure (pressures after maxima in G_{ex}).

3. does not undergo phase changes or rearrangements in the linear pressure interval at high pressure.

Furthermore, the dimension of the adsorbed molecule is assumed to be isotropic, meaning all sites have the same length. Equation 5.2.4 can be modified if the molecule is non-isotropic. A detailed explanation of this variation can be found in the film thickness chapter.

The method described here uses a different approach to obtain specific surface areas of a porous material. Instead of estimating the monolayer capacity n_{mono} from sub-monolayer data using theoretical subcritical model isotherms, such as BET isotherms, this method uses experimental conditions under which a true monolayer film covers the entire surface and determines the film volume $V_{\mathrm{sat.\ film}}$ instead of n_{mono}, which can be done without the need for any theoretical assumptions. Furthermore, instead of using a fixed molecule cross-sectional area σ, based on some theoretical packing model, such as liquid packing (BET theory), the film thickness $t_{\mathrm{sat.\ film}}$ is determined as an experimental quantity, as described in chapter 3, associated with the system (material and gas) under investigation and therefore is free of any theoretical assumptions.

The same cryogenic hydrogen isotherms used in earlier chapters have been analyzed according to the procedure as noted above and compared to the specific surface areas determined by BET theory from subcritical nitrogen isotherms.

Table 9 Comparison between specific surface areas calculated with BET theory (N_2 isotherm) and high pressure H_2 isotherms collected at 77 K.

Specific surface area $\left[\frac{m^2}{g}\right]$			
	BET theory	Average $\rho_{sat.\ film}$ 77 K*	$\sum_{BET} - \sum_{sat.\ film}$ [%]
HS;0B-20	936	752 ± 23	20
PVDC-412	1140	861 ± 39	24
PVDC-400	783	676 ± 9	14
PVDC-410	680	557 ± 13	18
PVDC-415	1200	955 ± 28	20
MSC-30	2760	2340 ± 68	15
3K-0079	2700	2010 ± 86	26
4K-245 (3.8 wt% boron)	2480	1830 ± 24	26
HKUST-1	2000	909 ± 26	55

*Uncertainties are calculated from spread of slope and film density

All specific surface areas calculated from the film density are consistently lower compared to the ones from BET theory. The discrepancy between specific surface areas determined from BET theory and those obtained from high pressure data is approximately 20%. This is puzzling because the hydrogen molecule is significantly smaller than a nitrogen molecule and therefore should be able to access additional surface sites. Thus, $\sum_{sat.\ film}$ from hydrogen should lead to larger values than $\sum_{BET}$. For example the study done by B. Streppel done on MOF MIL-101 shows a 9% increase in $\sum_{BET}$ obtained with hydrogen gas compared to the standard gas nitrogen[32].

The underestimation in specific surface area obtained from high pressure data was previously reported in literature[15]. Aranovich et al. determined the specific surface area from multiple high pressure data sets (nitrogen, krypton, methane) on GAC 250 activated carbon at 298

K in a similar fashion as described here[15]. Their values are also consistently lower than the ones calculated using BET theory. At this point it is not clear which method yields the "true" specific surface area of a porous material. For example, BET theory could overestimate the surface because of the number of micropores (< 2nm) present in the material. In small pores the adsorption potential overlaps from both sites creating a deeper potential well. Previous studies indicate that this effect can influence σ, leading to an exceptional large $\sum_{\mathrm{BET}}$ for microporous materials[22]. Furthermore, neutron diffraction and adsorption microcalorimetry studies done by Rouquerol et al. suggest that the nitrogen quadrupole orientation does depend on the surface structure. The author suggests, "nitrogen molecules are able to interact 'vertically' with surface hydroxyl groups", which degreases α, resulting in an overestimation of the specific surface area[22]. Because of the many sources for error associated with using BET theory to estimate the specific surface area, Rouqueroul suggests an uncertainty of ±20%[22].

With the exception of HKUST-1, all $\sum_{\mathrm{sat.\ film}}$ calculated from high pressure data are close to, or within the 20% uncertainty range of the values obtained from BET theory, suggesting the method and assumptions used for the new high pressure method are reasonable. All materials investigated in this report have a considerable number of micropores, which could explain to some extent the consistently lower surface area from high pressure data.

The $\sum_{\mathrm{BET}}$ for HKUST-1 is two times larger compared to that obtained by the method described here. As described in chapter 3, HKUST-1 has a heterogenic structure composed of metal sites (high binding sites) and organic linker molecules (low binding sites). Thus, the surface is not energetically homogeneous, which can lead to misleading values if the BET theory is used to evaluate the surface area. One of the assumptions made with BET theory is that there is a uniform monolayer on an energetically homogeneous surface. This is not true for HKUST-1,

therefore its calculated specific BET surface area is questionable, and that obtained by the "experimental" method is most likely more accurate.

The same high pressure analysis technique, as described earlier, was used to determine specific surface areas from high pressure hydrogen isotherms but the temperature was lowered to 50 K. The recorded measurements are the same as those used in earlier chapters, and the linear portion was separated into two sections (see figure 10). The earlier chapters describe in detail how $V_{\text{sat. film}}$ and $\rho_{\text{sat. film}}$ are determined.

Table 10 Specific H_2 surface areas calculated from high pressure isotherms recorded at 50 K.

	Specific surface area $\left[\frac{m^2}{g}\right]$			
	BET theory	Average $\rho_{\text{sat. film}}$*	1st linear regime*	2nd linear regime*
PVDC-412	1140	926 ± 135	1150 ± 10	883 ± 52
PVDC-410	680	653 ± 24	684 ± 8	638 ± 16
PVDC-415	1200	949 ± 168	1214 ± 7	851 ± 56
4K-245 (3.8 wt% boron)	2480	2480 ± 315	2940 ± 60	2310 ± 110

*Uncertainties are calculated from spread of slope and film density

The $\sum_{\text{sat. film}}$ obtained from the average value of the high pressure data has a comparable trend to the study conducted at 77 K. For the majority of materials, specific BET surface areas are larger than the ones obtained from high pressure linear regime. At such low temperatures, the isotherm exhibits two linear portions with slightly different slopes. Therefore the linear interval is broken up into two individual parts and separately analyzed. Specific surface areas calculated from the first high pressure section agree remarkably well with the ones from BET theory. With the exception of material 4K-245, the difference is less than ±1%, suggesting 50 K isotherms are well suited for this analysis if compared to BET theory. The outlier 4K-245, exhibits the opposite trend. Its first high pressure portion gives rise to a 19% higher specific surface area, and the second is 7% lower.

One reason for the discrepancy between $\sum_{BET}$ and the average value governed from method described here could be due to the number of data points recorded for each high pressure section. The first linear portion is shorter and therefore has lower data points compared to the second. Taking the average over the entire range therefore produces lower values. This effect can be compensated for if the average is calculated separately for each linear part and then these values are combined to get the overall average. By using this method the difference between the $\sum_{BET}$ and the $\sum_{sat.\ film}$ is ±14%, which is still in good agreement considering both linear portion of the isotherm are used.

The difference in specific surface areas calculated from high pressure isotherms at 77 K and 50 K cannot be explained by small variations of the adsorbent because each isotherm was recorded on the exact same sample. Hence it must be due to differences in the adsorbed film at each temperature, which seems to validate the conclusions made in chapter 2, that the adsorbed hydrogen film undergoes some sort of rearrangement between 50 K and 77 K. The method described here for calculating specific surface areas from supercritical high pressure adsorption isotherms shows promising results if cryogenic isotherms (≤ 77 K) are used. Unfortunately at this point it is not clear which cryogenic temperature should be used to analyze the adsorbed film because the true specific surface areas of the materials used in this study are unknown. Therefore the only possible way to test this new method is by comparing it with BET theory. Both temperatures gave $\sum_{sat.\ film}$ within 20%, meaning they are inside the estimated uncertainty of the BET theory[22]. By lowering the temperature to 50 K an excellent agreement (< 2%) between both methods was achieved. This is surprising because two different probing molecules, N_2 for BET respectively H_2 for high pressure isotherms, have been used but leading to the same outcome. Furthermore the method described here is based only on few assumptions (monolayer, isentropic molecule) and does not require the knowledge of the cross-sectional area of the

adsorbed molecule. In addition, it is simple to apply and no special adsorption instrument is needed. Any high pressure instruments capable of collecting cryogenic isotherm can be used.

5.3 Two layer BET theory

The materials studied here are mainly composed of micropores, meaning the majority of pores can only host a single or double layer of adsorbed gas. As mentioned before, typically subcritical low pressure nitrogen isotherms, in combination with BET theory, are used to calculate the specific surface area of porous materials. In classical BET theory, the adsorbed film is unrestricted, implying that it can form infinite layers under subcritical conditions. But this is not valid for microporous materials. These only allow a finite number of layers due to the narrow pores. Therefore, an attempt was made to modify the original theory to restrict the formation of layers to two. By setting N_{layer} equal to two, equation

$$\frac{n}{n_{\text{mono}}} = \frac{c\frac{P}{P_0}}{1-\frac{P}{P_0}} \frac{1-\left(N_{\text{layer}}+1\right)\left(\frac{P}{P_0}\right)^{N_{\text{layer}}}+N_{\text{layer}}(\frac{P}{P_0})^{N_{\text{layer}}+1}}{1+(c-1)\frac{P}{P_0}-c\left(\frac{P}{P_0}\right)^{N_{\text{layer}}+1}} \tag{5.4.1}$$

becomes

$$\frac{n}{n_{\text{mono}}} = \frac{c\frac{P}{P_0}}{1-\frac{P}{P_0}} \frac{1-3\left(\frac{P}{P_0}\right)^{2}+2(\frac{P}{P_0})^{3}}{1+(c-1)\frac{P}{P_0}-c\left(\frac{P}{P_0}\right)^{3}} \tag{5.4.2}$$

with n_{mono} equal to the monolayer capacity, P_0 equals the saturation pressure, and c is a constant related to the "net molar energy of adsorption". This leads to a BET equation similar to the original, with the exception of an additional negative cubic term.

$$\frac{\frac{P}{P_0}\left(1-3\frac{P}{P_0}^2+2\frac{P}{P_0}^3\right)}{n\left(1-\frac{P}{P_0}\right)}=\frac{1}{n_{\text{mono}}c}+\frac{c-1}{n_{\text{mono}}c}\frac{P}{P_0}-\frac{1}{n_{\text{mono}}}\left(\frac{P}{P_0}\right)^3 \tag{5.4.3}$$

The monolayer capacity, n_{mono}, and constant, c, can be evaluated by plotting the left hand side

$$\frac{\frac{P}{P_0}\left(1-3\frac{P}{P_0}^2+2\frac{P}{P_0}^3\right)}{n\left(1-\frac{P}{P_0}\right)} \tag{5.4.4}$$

versus pressure and fitting the cubic polynomial from the right hand side.

$$\frac{1}{n_{\text{mono}}c}+\frac{c-1}{n_{\text{mono}}c}\frac{P}{P_0}-\frac{1}{n_{\text{mono}}}\left(\frac{P}{P_0}\right)^3 \tag{5.4.5}$$

This is slightly different from the original theory, because both values (n_{mono}, c) are fitting parameters and do not need to be calculated from fitted parameters, such as slope and intercept.

One difference between classical BET theory and our modified version can be found by comparing their respective BET plots (Figure 24). For all materials tested in this report, the BET plot calculated with the two layer theory stays linear significantly longer than that of classical theory. Therefore, more experimental data can be used for the fit increasing its reliability.

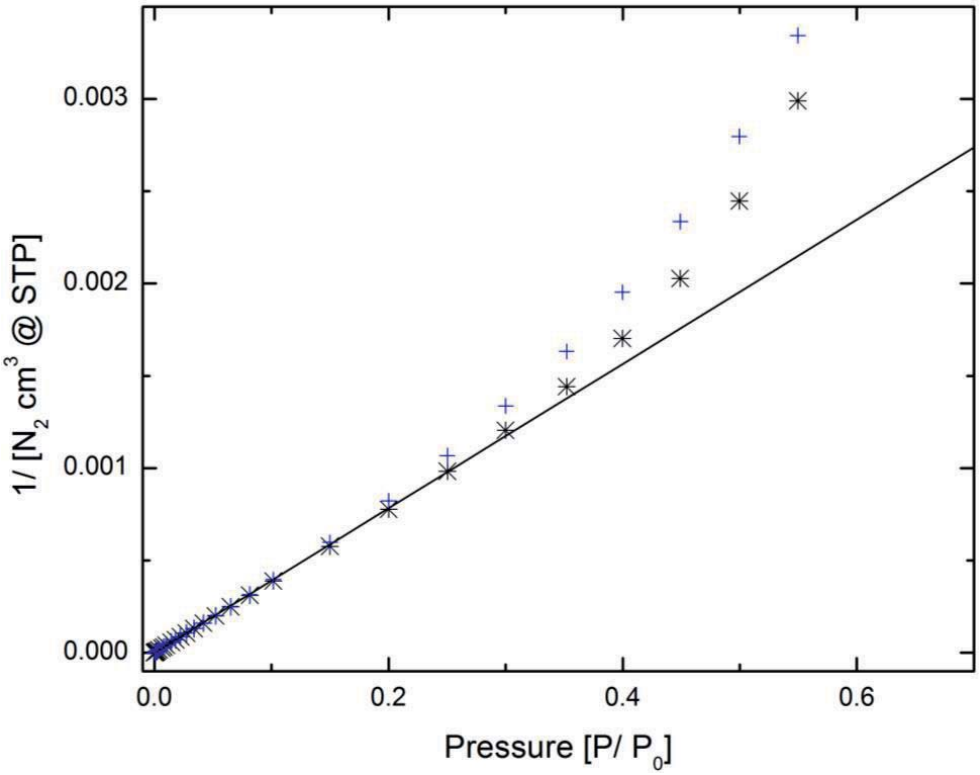

.

Figure 24 BET plots for a synthetic carbon (PVDC-412). The black stars are calculated with infinite layer and the blue crosses with 2 layer theory**.** The 2 layer departs at high pressure from linearity.

Comparing a theoretical two layer BET isotherm, with $c = 1000$, to the classical BET isotherm with the same parameters should shed some light how quickly the adsorbed film reaches saturation. The parameter $c = 1000$ was chosen because it is representative of typical values from synthetic carbons.

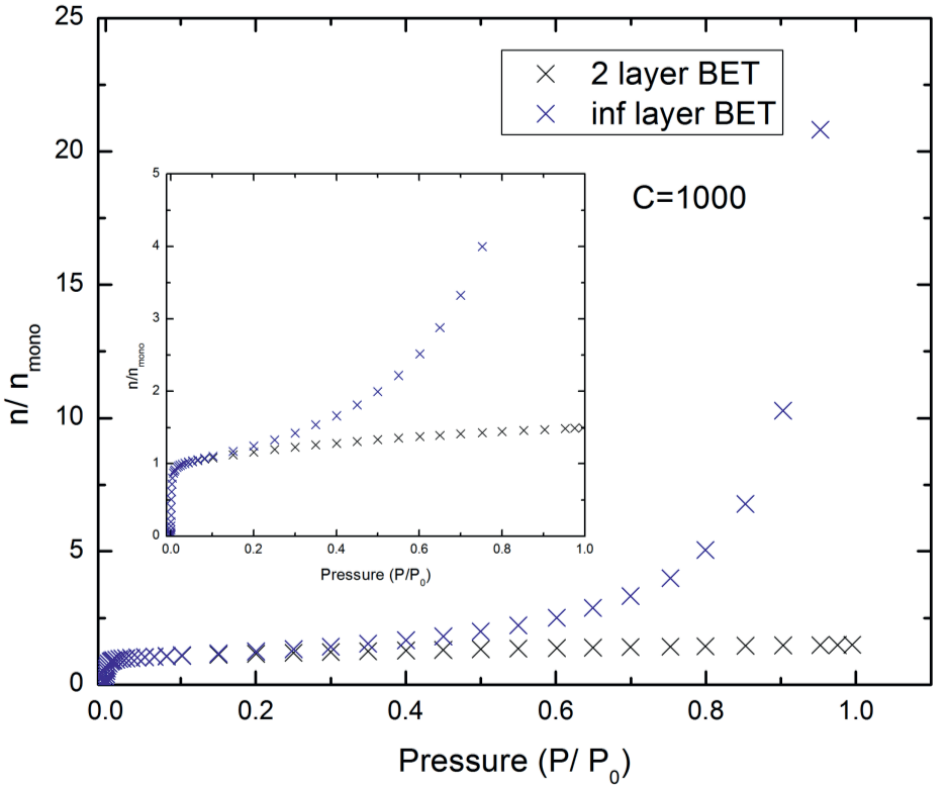

Figure 25 Number of layers formed with increasing pressure for finite and 2 layer BET model

The two layer theory resembles a type 1 isotherm (no inflection point) as long as c exceeds 1, which is not so for infinite BET theory, which leads to a type 2 isotherm (one inflection point) if c exceeds 2. This is expected due to the truncation of the film to two layers, meaning even at pressures close $P/P_0 = 1$ only two instead of infinite layers are allowed. It is expected that the restricted film reaches its maximum of two if the pressure is close to saturation ($P/P_0 = 1$), but near saturation it only reaches 1.5 layers (Figure 25).

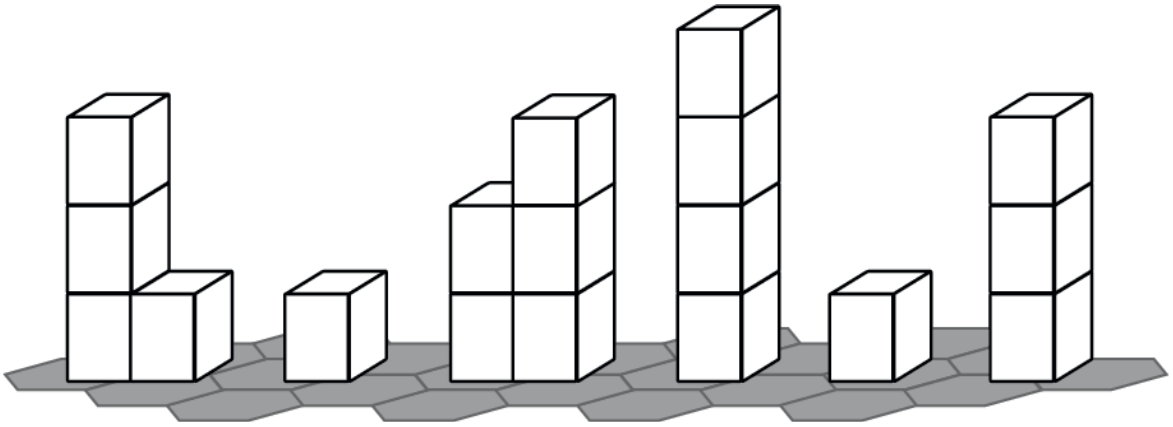

Figure 26 Schematics of adsorbed molecules described by BET theory. BET theory does not include adsorbate-adsorbate interactions, which can leads to unphysical film configuration.

One explanation could be due to the surface roughness of the adsorbed film. BET theory does not account for adsorbate–adsorbate interactions that allow two, adjacent adsorption sites, to have a significant different number of adsorbed layers. For example, one site could have no layers of adsorbed gas and the other have several layers. Consequently, the average number of layers is reduced. As expected, both theories complete a monolayer at similar pressures ($P/P_0 = 0.03$) and diverge afterwards. The classical theory starts increasing exponentially after the monolayer is filled, until it reaches its maximum at 210 layers. Varying c does not change the number of adsorbed layers if $c > 10$, but influences how quickly the first layer is filled because the isotherms from both models rise more steeply with increasing c. The shape of the isotherm seems to be independent of c after the completion of the monolayer.

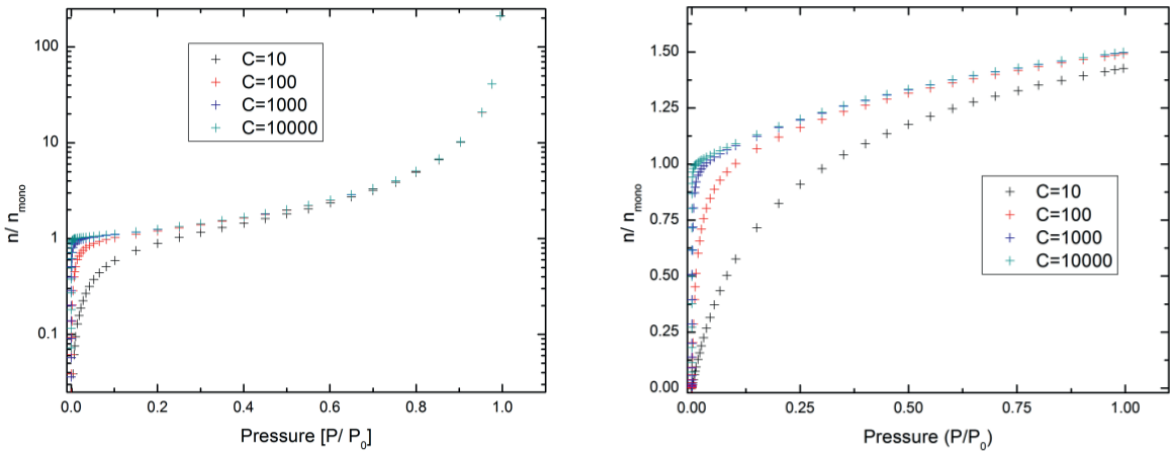

Figure 27 Graph of formation of layers for different BET c values. Left graph shows infinite layer model and right graph 2 layer model.

Five materials with different pore size distributions and surface chemistry have been analyzed with the 2 layer BET model and compared to the classical BET theory. The same seven data points of the subcritical nitrogen isotherm were used for the fits for the 0.008 – 0.03 P/P_0 pressure interval and 25 points for $7.78*10^{-6}$ – 0.065 P/P_0 respectively. With the exception of the lowest pressure interval, the same seven data points of the subcritical nitrogen isotherm were used for the fit.

Table 11 Specific surface areas calculate from infinite layer and two layer BET model at different pressure intervals.

	C value	Specific surface area $\left[\frac{m^2}{g}\right]$	Pressure interval $\left[\frac{P}{P_0}\right]$	R^2
PVDC-412				
2 layer BET	1970 ± 49*	1140 ± <1*	0.008 – 0.03	1
Inf. layer BET	2030 ± 41$^+$	1140 ± <1$^+$	0.008 – 0.03	1
2 layer BET	5670 ± 1240*	1130 ± 2*	$7.78*10^{-6}$ – 0.065	0.99993
PVDC-414				
2 layer BET	2270 ± 47*	811 ± <1*	0.008 – 0.03	1
Inf. layer BET	2340 ± 37$^+$	810 ± <1$^+$	0.008 – 0.03	1
2 layer BET	7080 ± 1500*	804 ± 1*	$7.78*10^{-6}$ – 0.065	0.99996
MSC-30				
2 layer BET	502 ± 56*	2770 ± 28*	0.008 – 0.03	1
Inf. layer BET	505 ± 56$^+$	2770 ± 29$^+$	0.008 – 0.03	0.999737
2 layer BET	1080 ± 308*	2800 ± 34*	$7.78*10^{-6}$ – 0.065	0.99641
4K-245				
2 layer BET	490 ± 52*	2490 ± 22*	0.008 – 0.03	1
Inf. layer BET	490 ± 52$^+$	2480 ± 25$^+$	0.008 – 0.03	1
2 layer BET	1040 ± 297*	2510 ± 32*	$7.78*10^{-6}$ – 0.065	0.99617
HKUST-1				
2 layer BET	7460 ± 5570*	2000 ± 5*	0.018-0.063	0.99996
Inf. layer BET	26400 ± 54600$^+$	2000 ± 4$^+$	0.018-0.063	0.999985
2 layer BET	33500 ± 14200*	2000 ± 1*	$7.78*10^{-6}$ – 0.065	0.99999

* from fit

+ from error propagation

Both theories resemble equal $\sum$ if applied to the same pressure interval, independent of the nature of surface chemistry or pore size distribution. The only difference can be found in the BET c value for the synthetic carbons PVDC-412 and PVDC-414. The classical infinite layer model gives a 3% higher value compared to the two layer one, which is within the uncertainty of the procedure and is therefore not relevant. MOF HKUST-1 exhibits vastly different c values depending on the chosen model. The two layer theory gives rise to 7460, compared to 26400 for the infinite theory. Both uncertainties calculated from error propagation (infinite model) and from the fit for the 2-layer model respectively are also very large. The error for the two layer model is even twice as large for the classical theory. Selecting other pressure intervals did lead to drastically different values but gave similar specific surface areas. The carbon-based materials (synthetic carbons, chemically activated carbons) do not exhibit such behavior, indicating how unstable c is for materials with an energetically heterogeneous surface.

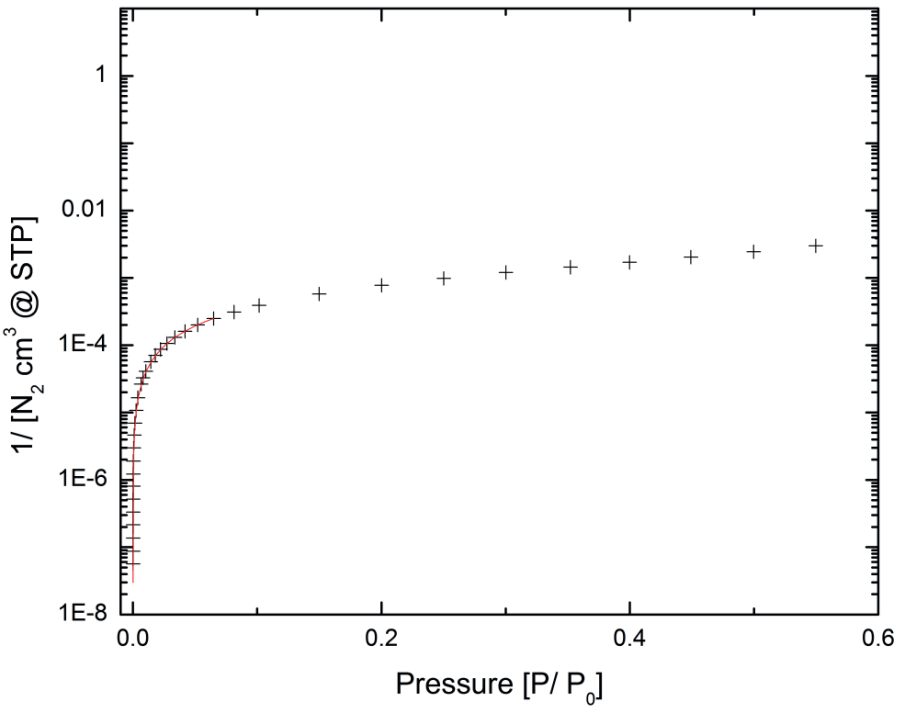

Figure 28 BET plot with the fitted "knee" at low pressure.

For the materials investigated in this report, all two layer BET plots exhibit a “knee” at low pressure if plotted on a semi-log scale. The third row of each material in Table 11 represents $\sum$ calculated by fitting the two layer model to this feature. These areas are comparable to both the infinite and two layer ones at higher pressures. Even HKUST-1 exhibits the same specific surface area if the “knee” is used for the fitting. This shows the two layer model gives comparable specific surface areas to the classical model if the “knee” is used for the fit, independent of the material under investigation. Thus, the question of which pressure interval should be used for the BET fit seems to be straight forward. The two layer theory gives the same $\sum$ independent of the materials chemical or pore structure as long as the knee at low pressure is used for the fit. The only difference can be found in the c values, which are considerably higher.

5.4 C value BET Theory

BET theory can be derived in two ways. Steele treated it in terms of statistical mechanics and showed that the grand partition function can be solved[33]. He arrives at the same mathematical formula (Equation 5.4.1), but in this case the BET constant, c, is related to the partition function of the first adsorbed layer, q_1, divided by the partition function of the higher layers, q_l, which are assumed to be the same as the bulk liquid.

$$c = \frac{q_1}{q_l} \tag{5.5.1}$$

On the other hand, Brunauer, Emmett, and Teller first derived the theory from a kinetic model. In this case c is proportional to the net molar energy of adsorption between the first adsorbed layer and the following layers ($q_1 - q_l$), which are assumed to be in the liquid state, the condensation coefficients, a_1 and a_2, and the vibrational frequencies normal to the surface, v_1 and v_2. The model assumes every layer above the first has the same properties, and for practical purposes A is usually set to unity. A more detailed explanation can be found in Rouquerol's book, Adsorption by Powders and Porous Solids[22,23].

$$c = A\mathrm{e}^{\frac{(q_1 - q_l)}{\mathrm{R}T}};\ \text{with}\ A = \frac{a_1 v_2}{a_2 v_1} \tag{5.5.2}$$

An increase in c should consequently be correlated to higher net molar energy of adsorption if the same conditions are used in each experiment. This correlation can be tested if the isosteric heat of adsorption of different materials is compared with their corresponding BET c values because the isosteric heat of adsorption is a measurement of the energy of adsorption. Five materials with different specific surface areas and chemistry have been chosen, and their isosteric heat of adsorption was compared with their BET c value(Figure 29). The isosteric heat of adsorption was evaluated according to the procedure mentioned in chapter 2.

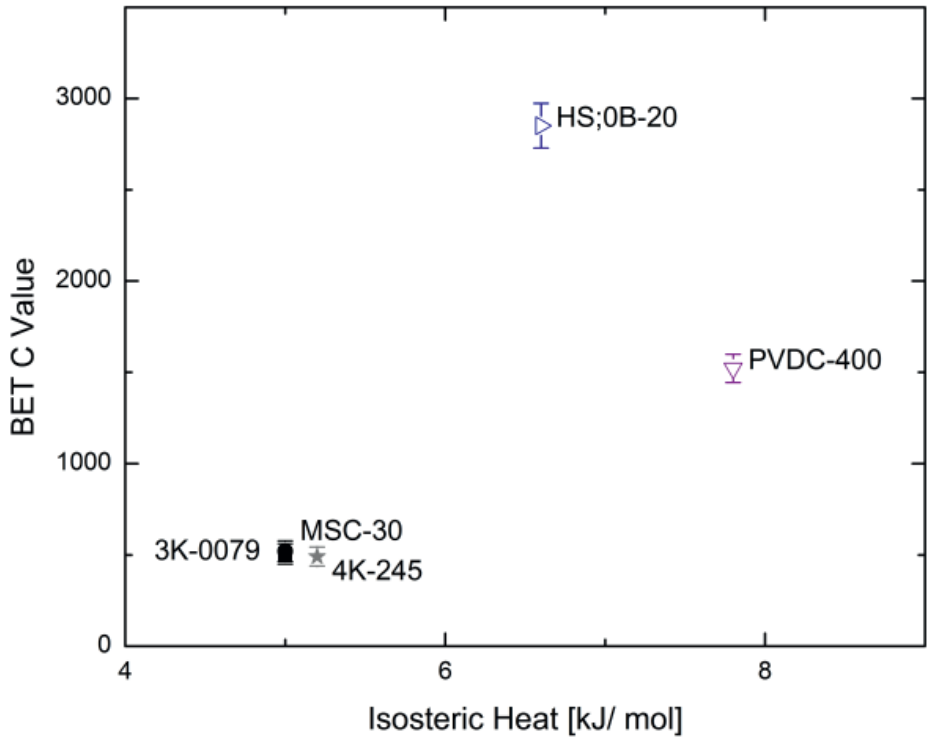

Figure 29 The graph shows BET c values calculated with the infinite layer model and the isosteric heat of adsorption.

There is not a strong correlation between both values (Figure29). All chemically activated materials lead to similar isosteric heat of adsorption of around 5 kJ/mol and *c* values around 500, respectively. This is expected if both values are related, but the boron doped material, 4K-245, has a slightly increased adsorption energy compared to chemically activated carbons but does not exhibit a larger *c* value. Conversely, synthetic carbons (PVDC-400, HS;0B-20), which show an increased isosteric heat of adsorption, do exhibit an increase in *c*. Strangely, the adsorbent with the highest *c* value (HS;0B-20) is not the one with the strongest adsorption energy. It seems there is a weak correlation between both values but it cannot be used to draw definite conclusions from it.

As mentioned in the introduction of this study, the adsorption potential in narrow pores is much deeper due to the superposition of the potentials from the surrounding walls. This lead to the question of whether the BET *c* value is influenced by narrow pores. For a variety of materials

subcritical nitrogen isotherms have been collected on an automated gas analyser (Autosorb-1 from quantachrome), and the BET c value is calculated from classical theory. Furthermore, the individual pore volume coming from pores with different sizes has been obtained with quenched solid density function theory (QSDFT), meaning how much pore volume comes from pores with a certain width (pore volume histogram). The standard software packet provided with the Autosorb-1 instrument was used to determine the pore volume histogram. Each pore volume for the respective pore size interval was then plotted versus the BET c value and examined for a correlation.

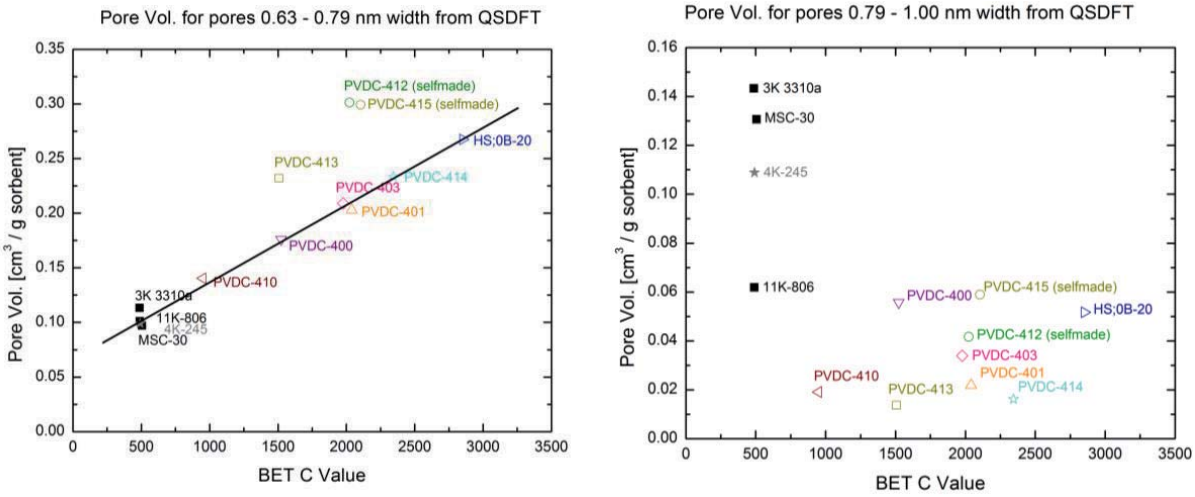

Figure 30 Correlation between calculated BET c values and pore volumes from different pore sizes. The graphs show the correlation between the pore volume due to pores < 0.79 nm (left) and pores of 0.79 - 1.0 nm (right) width and the material's BET c value.

Only the plot for pores with a width between 0.63 – 0.79 nm indicated a correlation between pore volume and c (Figure 30 left). Every other plot leads to a more or less random distribution. Regardless of whether the material is chemically activated carbon, synthetic carbon, or if the surface is doped with boron, they exhibit a linear correlation between the pore volume coming from sub-nanometer pores and c. Only four materials of the thirteen do not have a strong correlation between sub-nanometer pore vol. and c. One of the reasons could be due to the QSDFT itself, which does not allow the user to account for a mixture of pore geometries. For this

type of analysis, the pore geometry needs to be specified for the QSDFT kernel. The software version used (Version 1.55) had only the option for slit shaped pores, which does not fully represent the true pore geometries of some of the samples. In particular, synthetic carbons can have a significant number of pores with various shapes due to the release of gaseous HCl during the manufacturing process. Another uncertainty comes from the QSDFT fit itself. The method tries to fit isotherms calculated from QSDFT with a variety of different pore sizes to the experimental data, and from this fit it determines the pore histogram. This, together with the chosen pore geometry, could lead to the discrepancy seen for some of the materials.

Chapter 6 - MU-7K CCHeR Sieverts apparatus

6.1 Design and theory

There are two common methods to record equilibrium sorption isotherms. The first one, usually referred as gravimetry, records the change in mass of the adsorbing material following a step change in gas pressure to calculate the amount of adsorbed gas (excess adsorption). Another common way to get the same quantity is called volumetry, or manometry. It monitors the change in gas pressure of a closed system (fixed volume). This is also known as the Sieverts' method, named after the German chemist Adolf Sieverts[34]. Both approaches have their advantages and disadvantages. For example, buoyancy effects play a major role in gravimetry and the poor thermal conductivity between adsorbent and the surrounding thermal bath[22,35]. This is most critical if the experiment is carried out at cryogenic temperatures on materials exhibiting low densities. In case of manometry, the systems internal volumes including the volume of the adsorbent (dead space) need to be precisely determined and any occurring thermal gradient between sample side and the rest of the apparatus must be accounted for.

For practical reasons, the manometric method is more often used because the loading of sensitive materials is not as cumbersome. Furthermore, the required technology, such as high precision pressure transducers, is readily available, and the basic layout of the instrument consists of two known volumes, referred as dosing volume (V_{d}) and reactor volume (V_{r}), with a valve separating them, which makes it the preferred method for home-made instruments. A detailed explanation on how to record an isotherm and calculate the excess adsorption is given later in this chapter.

Commercially available manometric gas adsorption instruments are commonly designed for very specific tasks and can be categorized into two classes. The more common class is designed to determine sample properties such as surface areas, porosity, and pore size distributions from

subcritical isotherms. The other class measures excess adsorption at high pressures (typically 100 or 200 bar) and various temperatures. It is mutual for most commercial instruments to use a thermal bath to control the sample temperature. Typically, a liquid nitrogen bath in combination with a heating jacket is used to control the temperature, which limits the working temperature to a minimum of 77 K, while the maximum temperature is limited by the heating jacket. The major drawback of this design is the small useful temperature range and the limited time for each isotherm due to the evaporating liquid nitrogen.

The instrument MU-7K CCHeR was designed to overcome some of the restrictions mentioned above. It is based on the manometric method (Sieverts' method) and uses a closed cycle He refrigerator instead of a thermal bath to control the sample temperature from 7 K to room temperature. The wide temperature range allows acquiring both sub- and supercritical isotherms for various gases and therefore permits, in addition to excess adsorption, studying sample properties such as BET surface area and porosity if a low pressure transducer is used.

The main body, including the sample reactor is made of 316 stainless steel parts and metal gasket face sealed fittings (VCR©, Swagelok) are used to connect individual portions of the instrument. The size of the reactor can be varied by using different sizes of VCR© bodies and can be up to 0.8 cm^3

Two pressure transducers, one for pressures up to 200 bar (UNIK 5000 from GE) and one for low pressures (<2 bar, Super TJE Ultra from Sensotec), are used to collect pressure readings. During high pressure measurements, the two bar transducer is disconnected from the system by closing a valve because it cannot withstand high pressures.

For experiments performed at temperatures lower as room temperature, the sample reactor can be mounted on a copper enclosure which is fixed to the cold finger of a closed cycle

He refrigerator (CCR) from Janis Research Co, inc. Two calibrated silicon diodes (DT-670, Lakeshore), one on the top and one on the bottom, of the copper enclosure are used to monitor the temperature and are connected to the temperature controller (Model 335, Lakeshore) of the CCR.

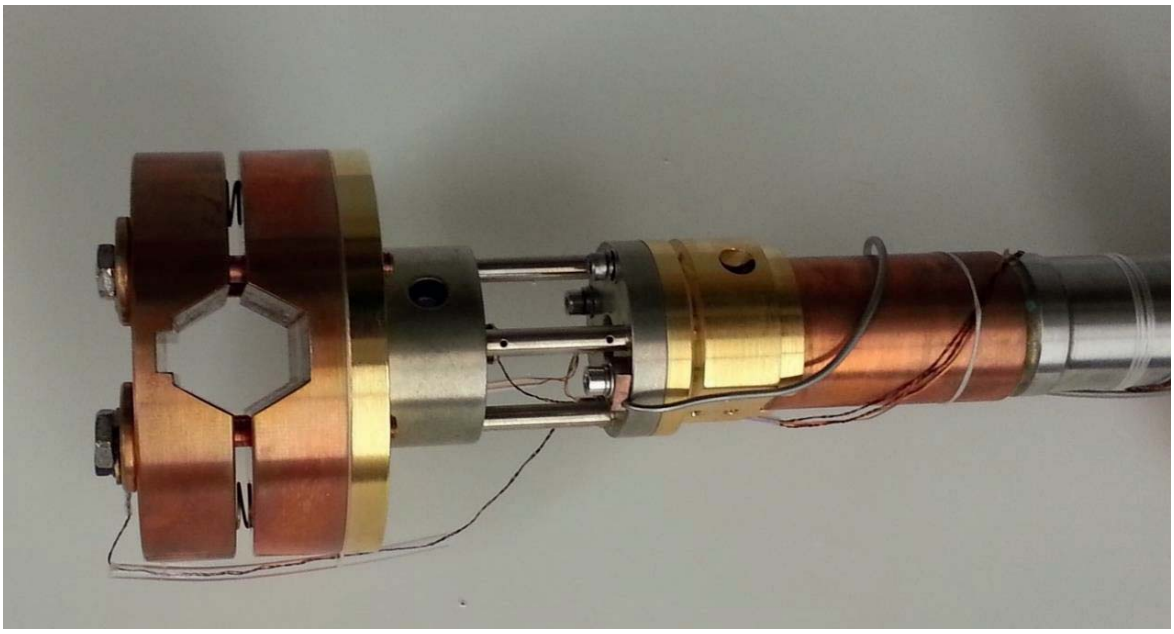

Figure 31 Sample mount on the top stage of the closed cycle refrigerator.

It guarantees that the material under investigation is at a well-known temperature and the size of the copper block ensures any heat produced during the exothermic process of adsorption can quickly dissipates away from the reactor. Unlike with the technique of a thermal bath, this method does not require keeping track of how much of the liquid evaporates and therefore changes the cold volume fraction from the reactor during the experiment. In addition, there are two high precision platinum resistance temperature detectors (RTD, Omega P-L-1/10-1/8-6-0-P-3) for monitoring gas temperatures inside the dosing volume. One is mounted such, that the tip is in direct contact with the gas inside the dosing volume. All valves are pneumatic valves to ensure no parasitic heat is introduced to the instrument. Solenoid driven valves introduce heat to the system if they are operated due to the current flowing through the solenoid. This leads to temperature instabilities in the gas system since they are directly connected to the gas filled

volumes. Furthermore it ensures that the gas handling site is separated from the electronics in case of a gas leak in the system. This is especially important if flammable gases are used for the experiments because it minimized the risk of a sudden combustion in case of a leak. The dosing volume V_d is in a sealed Plexiglas box to ensure temperature changes in the room do not affect the measurement and a capillary tube with an inner diameter of less than a millimeter is used to connect both volumes V_d and V_r. This minimizes the amount of gas exposed to the laboratory temperature and reduces the dead volume of the reactor side. To ensure an autonomous operation, all pneumatic valves are driven by solenoid valves which are connected to a computer in addition to the temperature detectors and pressure transducers. A computer program, written in Labview, is used to control the instrument and collect the data automatically.

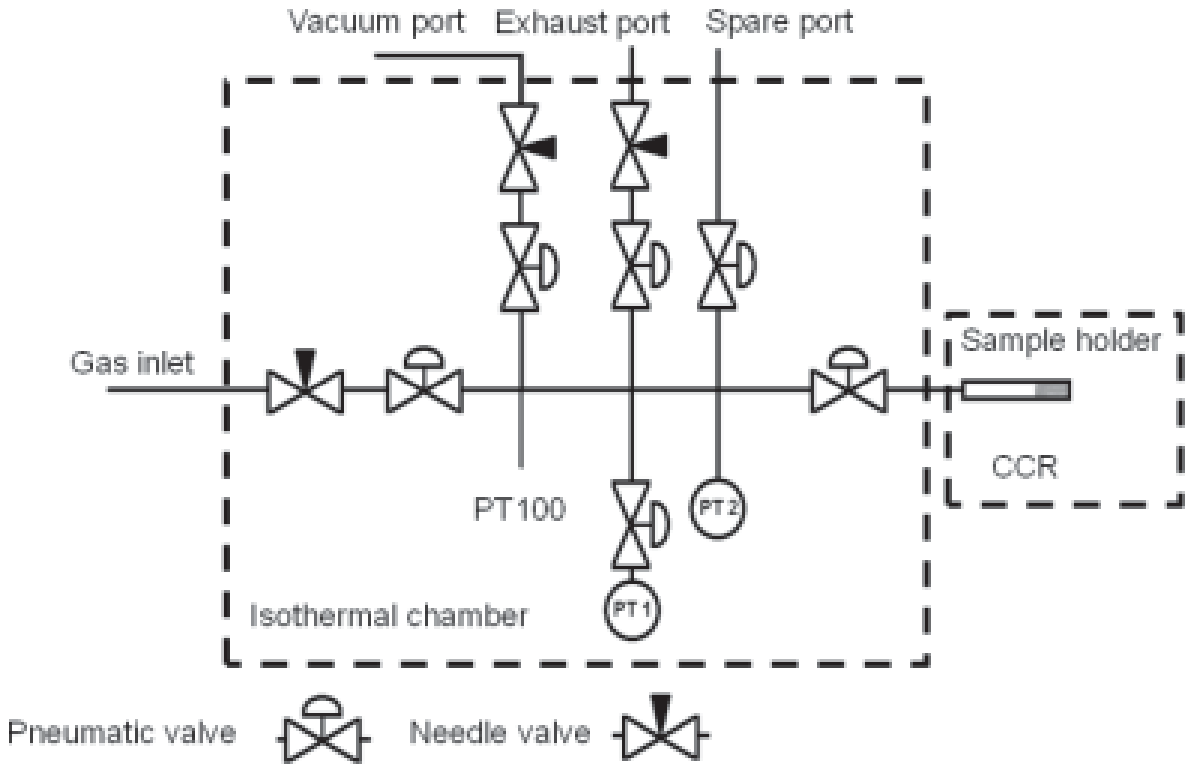

Figure 32 The schematic of the high pressure manometric gas adsorption instrument MU-7K CCHeR.

The MU 7K CCHeR instrument uses the pressure drop occurring after the gas expands into the sample to determine excess adsorption. Prior to an experiment, the entire system

including adsorbent is outgassed. In the first step the adsorbing gas is introduced into the evacuated dosing volume V_d and allowed to equilibrate. Under the assumption of conservation of particle number, the mass density $\rho(P_{\mathrm{I}i}, T_{\mathrm{I}i})$ is determined from the temperature and pressure using an appropriate equation of state (EOF). The first subscribed stand for the step in the procedure and the second one for the point in the isotherm. For this study the EOF from the program REFPROP, provided by the National Institute of Standards and Technology (NIST), was used. After equilibrium is reached, the adsorbate is introduced into the reactor volume by opening the valve separating both volumes. Again, after equilibrium is reached, the gas density $\rho(P_{\mathrm{II}i}, T_{\mathrm{II}i})$ is calculated from the pressure and temperature and the excess adsorption is given by

$$m_\mathrm{ex} = V_\mathrm{d}(\rho(P_{\mathrm{I}i}, T_{\mathrm{I}i}) - \rho(P_{\mathrm{II}i}, T_{\mathrm{II}i})) - \rho(P_{\mathrm{II}i}, T_{\mathrm{II}i})(V_\mathrm{r} - V_\mathrm{s}) \tag{6.1.1}$$

with V_s representing the skeletal volume (sum of the skeletal and open pore volume) of the material under investigation. The remaining gas m_i in V_d needs to be known for an experiment with multiple data points to avoid double counting. Therefore the valve separating both volumes is closed and the gas density $\rho(P_{\mathrm{III}i}, T_{\mathrm{III}i})$ obtained.

$$m_i = V_\mathrm{d}\big(\rho(P_{\mathrm{I}i}, T_{\mathrm{dI}i}) - \rho(P_{\mathrm{III}(i-1)}, T_{\mathrm{dIII}(i-1)})\big) \tag{6.1.2}$$

The procedure can be repeated to acquire multiple data points and the excess adsorption is then represented by

$$m_\mathrm{ex} = \sum_{i=1}^{N}\left[\rho(P_{\mathrm{I}i}, T_{\mathrm{dI}i}) - \rho(P_{\mathrm{III}(i-1)}, T_{\mathrm{dI}(i-1)})\right]V_\mathrm{d} - \rho(P_\mathrm{II}, T_\mathrm{dII})\,[V_\mathrm{d} + V_\mathrm{r} - V_\mathrm{s}] \tag{6.1.3}$$

Normalizing m_ex to the mass of the material under investigation, leads to the gravimetric excess adsorption.

$$G_\mathrm{ex} = \frac{m_\mathrm{ex}}{m_\mathrm{s}} \tag{6.1.4}$$

If a study is conducted in which the reactor is kept at a temperature different from the dosing volume, then it is necessary to split the reactor volume into two volumes, one is at the same temperature as the dosing volume and the other at the sample temperature. This ensures that the gas densities inside the reactor are represented correctly and is especially important for experiments at cryogenic temperatures such as 77 K. The volume faction is represented by the factor f ($0 \leq f \leq 1$), with $f = 1$ meaning the entire reactor is at the same temperature as the sample. The room temperature reactor volume is now given by $V_\mathrm{r}(1-f)$ and the cold part is represented by $V_\mathrm{r}f$. A detailed explanation on how to determine f is given in a alter chapter. Finally, gravimetric excess adsorptions is given by

$$G_\mathrm{ex}:=\frac{m_\mathrm{ex}}{m_\mathrm{s}}=\sum_{i=1}^{N}\left[\rho(P_{\mathrm{I}i},T_{\mathrm{dI}i})\ -\rho(P_{\mathrm{III}(i-1)},T_{\mathrm{dI}(i-1)})\right]V_\mathrm{d}-\rho(P_\mathrm{II},T_\mathrm{dII})\ [V_\mathrm{d}+V_\mathrm{r}(1-f)] \\ -\rho(P_\mathrm{II},T_\mathrm{sII})[V_\mathrm{r}f-V_\mathrm{s}] \tag{6.1.5}$$

m_ex: Mass of adsorbed gas [g]

m_s: Mass of adsorbent [kg]

$\rho(P_{\mathrm{I}i},T_{\mathrm{dI}i})$: Initial gas density in dosing volume at dosing temperature [g/ L]

$\rho(P_{\mathrm{III}(i-1)},T_{\mathrm{dI}(i-1)})$: Final gas density in dosing volume at dosing temperature (closed sample valve) [g/ L]

$\rho(P_\mathrm{II},T_\mathrm{dII})$: Gas density (open sample valve) at dosing temperature [g/ L]

$\rho(P_\mathrm{II},T_\mathrm{sII})$: Gas density (open sample valve) at sample temperature [g/ L]

V_d: Dosing volume [cm^3]

V_r: Reactor volume [cm^3]

V_s: Sample volume [cm^3]

f: Volume fraction of V_r which is at sample temperature

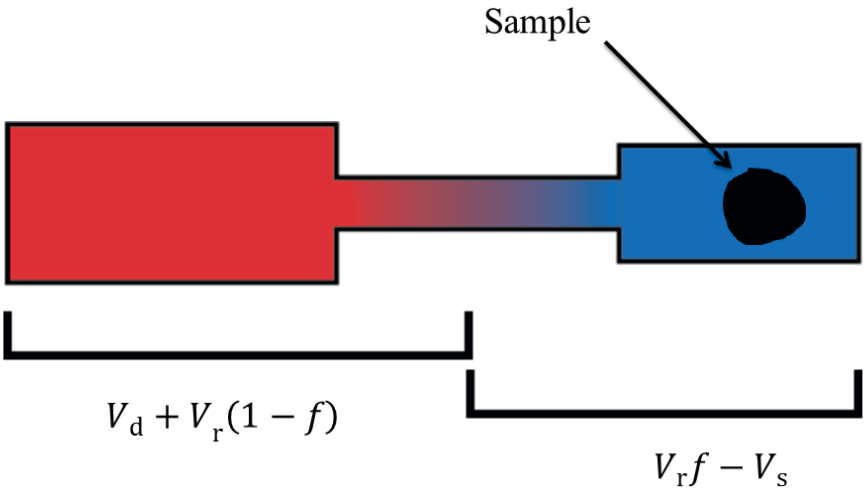

Figure 33 Schematic representation of the volumes and their associated temperatures.

On consequence of the procedure is the dependency of each data point from all prior ones. Thus, the uncertainty accumulates with increasing number of data points. However, the uncertainty does not strictly add up, because only the expression in the summation (equation 6.1.5) depends on previous data. One method to avoid the accumulation of uncertainty is by bringing the system back to vacuum between each data point. This reduces the required density measurement ($\rho(p_{\mathrm{III}(i-1)}, T_{\mathrm{III}(i-1)})$ is eliminated) by one because it eliminates the step of keeping track of m_i.

6.2 Skeletal density

Prior to each experiment, the remaining volume of the reactor which is not occupied by the adsorbent (dead space volume) needs to be determined. There is an indirect and direct method to obtain it. The direct method is preferred by many commercially available adsorption instruments because it can be used to simultaneously obtain V_s and what fraction of V_r is at a different temperature compared to the rest of the instrument. It is usually done by expanding a known volume of He gas into the reactor, filled with the adsorbate. The drop in pressure occurring is then used to estimate the dead space volume. This method assumes no adsorption occurs. A more detailed procedure can be found in Rouquerol's adsorption book[22]. The use of He to determine the dead space volume dates back to Washburn and is adopted by many adsorption instruments[36]. In the majority of experimental measurements, He calibration is performed either at the temperature of the experiment, such as 77 K, or at room temperature. He is used because it is believed to be a non-adsorbing gas. Unfortunately recent studies show this is not the case for highly porous materials, and the effect can observed both at cryogenic and room temperature[37,38]. This problem is especially important for automated gas adsorption instruments because they do not provide an easy method to test if the obtained dead space volume is correct. When a sample adsorbs He, the sample appears to displace less He as it would in the absence of adsorption, and the skeletal volume appears to be smaller, resulting in a decrease of excess adsorption.

If the volume of the adsorbent material is known, an indirect approach can be used to determine the dead space volume. There are two ways to obtain the volume:

1. The volume can be estimated from the theoretical density of the material. This is the preferred method for crystalline materials such as metal organic frameworks because

their crystal structure can be determined from x-ray diffraction or simulations. Unfortunately, this method leads to a volume which includes pores inaccessible to the adsorbate, such as closed pores.

2. Pycnometry measurement done with gas or liquid can be used to obtain the materials volume. This leads to a volume which does not include inaccessible space such as closed pores and thus is better suited for adsorption studies. It is crucial to verify no adsorption takes place if the study is carried out with a gaseous medium. The simplest way to check if adsorption takes place is, by collecting several data points at different pressures. Adsorption can be ruled out only if they lead to the same volume.

If possible pycnometry measurements should be the first option to obtain skeletal volume of an unknown material because it is consistent with the volume seen by an adsrobate, provided that the adsorbate molecule is similar in size to the probing molecule. In addition to the true sample volume, it is straight forward to check weather adsorption took place during the measurement, which increases the confidence of the obtained value.

Due to the majority of similar materials investigated in this study and the exhaustive nature of accurate He pycnometry measurements, it is impractical to determine skeletal densities for each sample individually. For these reasons, the skeletal density of representative materials have been measured with He (room temperature) and then applied to all materials of the same class. For example, the carbon based materials (chemically activated carbon, synthetic carbon) gave rise to a skeletal density of ρ_{skel} = 2.04± 0.03 mL with no adsorption observed(Figure 34).

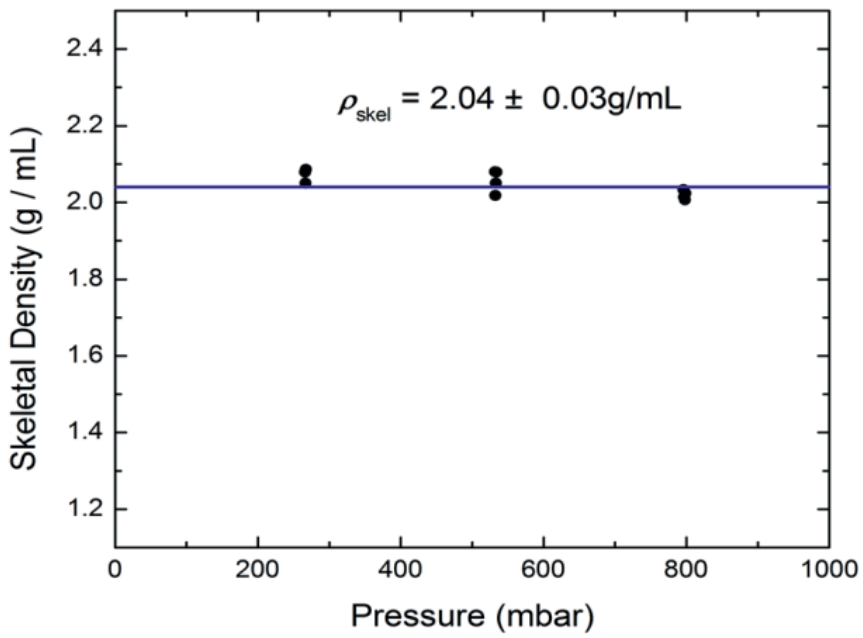

Figure 34 Skeletal density measurement (He) for an activated carbon sample by applying Eq.(XX) in conjunction with the definition of skeletal density $\rho_{\mathrm{skel}} = m_{\mathrm{s}}/V_{\mathrm{s}}$. No He adsorption was observed during this experiment.

6.3 Volume Determinations & Quality of Measurements

The formulation of the above excess equations was based on the assumption that all volumes were known. This chapter outlines the process used to calibrate the dosing volume and, reactor volume. Assuming that neither the dosing nor reactor volumes are known, three sets of measurements are required:

1. 15 individual data points with no sample
2. 15 individual data points with a non-adsorbing sample of known volume. In this case silicon beads with a known density of $\rho_{\mathrm{Si}} = 2.3290\ \mathrm{g/cm^3}$
3. A blank isotherm at room temperature

For the fifteen individual data points with no sample, equation 6.1.1 can be used by setting $V_{\mathrm{s}} = 0$ and using f to increase the precision. It is crucial to use f for the volume determination because even a slight temperature difference in the system leads to large uncertainties in Volume.

$$\rho(P_{\mathrm{I1}}, T_{\mathrm{dI1}})V_{\mathrm{d}} = \rho(P_{\mathrm{II1}}, T_{\mathrm{dII1}})[V_{\mathrm{d}} + V_{\mathrm{r}}(1-f)] + \rho(P_{\mathrm{II1}}, T_{\mathrm{sII1}})V_{\mathrm{r}}f \qquad (6.3.1)$$

where the additional subscript "1" has been added to indicate measurements taken with no sample and subscript "2" with the volume displacer. For the fifteen individual data points with non-adsorbing sample of known volume, conservation of particle number gives

$$\rho(P_{\mathrm{I2}}, T_{\mathrm{dI2}})V_{\mathrm{d}} = \rho(P_{\mathrm{II2}}, T_{\mathrm{dII2}})[V_{\mathrm{d}} + V_{\mathrm{r}}(1-f)] + \rho(P_{\mathrm{II2}}, T_{\mathrm{sII2}})\left[V_{\mathrm{r}}f - V_{\mathrm{disp}}\right] \qquad (6.3.2)$$

where V_{disp} is the volume of the displacer. Solving the system of Eqs. (6.3.1) and (6.3.2) gives the dosing and reactor volumes

$$
\begin{aligned}
V_{\mathrm{r}} = \; & (\rho(P_{\mathrm{II2}}, T_{\mathrm{sII2}})[\rho(P_{\mathrm{II1}}, T_{\mathrm{dII1}}) \\
& - \rho(P_{\mathrm{I1}}, T_{\mathrm{dI1}})]\, V\_\mathrm{disp})/(\rho(P_{\mathrm{II1}}, T_{\mathrm{dII1}})\rho(P_{\mathrm{I2}}, T_{\mathrm{dI2}}) \\
& - \rho(P_{\mathrm{II2}}, T_{\mathrm{dII2}})\rho(P_{\mathrm{I1}}, T_{\mathrm{dI1}}) + f\,[\rho(P_{\mathrm{II1}}, T_{\mathrm{dII1}})\rho(P_{\mathrm{II2}}, T_{\mathrm{sII2}}) \\
& + \rho(P_{\mathrm{II2}}, T_{\mathrm{dII2}})\rho(P_{\mathrm{I1}}, T_{\mathrm{dI1}}) - \rho(P_{\mathrm{II2}}, T_{\mathrm{dII2}})\rho(P_{\mathrm{I1}}, T_{\mathrm{dI1}}) \\
& - \rho(P_{\mathrm{II1}}, T_{\mathrm{dII1}})\rho(P_{\mathrm{I2}}, T_{\mathrm{dI2}}) + \rho(P_{\mathrm{II1}}, T_{\mathrm{sII1}})[\rho(P_{\mathrm{I2}}, T_{\mathrm{dI2}}) \\
& - \rho(P_{\mathrm{II2}}, T_{\mathrm{dII2}})]]\,)
\end{aligned}
\tag{6.3.3}
$$

$$
\begin{aligned}
V_{\mathrm{d}} = \; & (\rho(P_{\mathrm{II2}}, T_{\mathrm{sII2}})[\rho(P_{\mathrm{II1}}, T_{\mathrm{dII1}})(f-1) \\
& - f\rho(P_{\mathrm{II1}}, T_{\mathrm{sII1}})]\, V_{\mathrm{disp}})/(\rho(P_{\mathrm{II1}}, T_{\mathrm{dII1}})\rho(P_{\mathrm{I2}}, T_{\mathrm{dI2}}) \\
& - \rho(P_{\mathrm{II2}}, T_{\mathrm{dII2}})\rho(P_{\mathrm{I1}}, T_{\mathrm{dI1}}) + f\,[\rho(P_{\mathrm{II1}}, T_{\mathrm{dII1}})\rho(P_{\mathrm{II2}}, T_{\mathrm{sII2}}) \\
& + \rho(P_{\mathrm{II2}}, T_{\mathrm{dII2}})\rho(P_{\mathrm{I1}}, T_{\mathrm{dI1}}) - \rho(P_{\mathrm{II2}}, T_{\mathrm{dII2}})\rho(P_{\mathrm{I1}}, T_{\mathrm{dI1}}) \\
& - \rho(P_{\mathrm{II1}}, T_{\mathrm{dII1}})\rho(P_{\mathrm{I2}}, T_{\mathrm{dI2}}) + \rho(P_{\mathrm{II1}}, T_{\mathrm{sII1}})[\rho(P_{\mathrm{I2}}, T_{\mathrm{dI2}}) \\
& - \rho(P_{\mathrm{II2}}, T_{\mathrm{dII2}})]]\,)
\end{aligned}
\tag{6.3.4}
$$

The correct volumes are obtained by changing f until the excess adsorption of the blank room temperature isotherm is minimized.

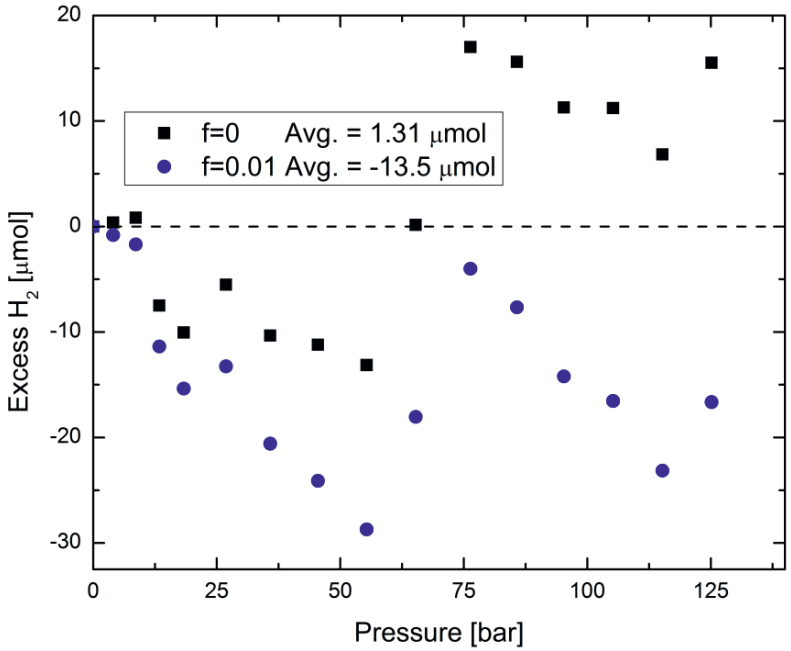

Figure 35 Blank isotherm at 296 K with f = 0 and f = 0.01. The fractional volume is decreased until the average departure from zero in the blank isotherm is minimized.

Figure 35 show a typical blank isotherm at room temperature which was used during the calibration process it yielded a dosing volume of $V_{\mathrm{d}} \cong 16.67 \pm 0.03$ mL and a reactor volume of $V_{\mathrm{r}} \cong 7.78 \pm 0.001$ mL. The blank isotherm shows a maximum departure from zero excess adsorption of approximately 16μmol, which is well below the tolerance of 40 μmol, indicating a proper calibration.

The above calibrations allow one to take isothermal measurements at the same temperature as the laboratory environment.

6.4 Fractional volume determination

As mentioned earlier, it is crucial for the density determination to know what portion of the gas in the instrument is at what temperature. This can be neglected only for studies performed at room temperature, if the entire system is at the same temperature.

In the case of the MU-7K CCHeR instrument f is determined by measuring an empty isotherm at the desired temperature and pressures. The parameter f is then changed to minimize the average excess adsorption. It can be assumed that the excess adsorption is equal to zero because no adsorbent is present, meaning the entire isotherm should measure zero. This is only valid if all volumes are correct; therefore any deviation from zero in excess adsorption has its origin in an incorrect determined volume. f can now be used for recording isotherms at this temperature. Instead of an entire isotherm, single doses can be used to estimate f more precise. A typical blank hydrogen isotherm at 77 K for the MU-7K CCHeR instrument does not differ more than 21 µmol from zero. The maximum departure from zero excess hydrogen is much larger at 77 K compared to the departure at 296 K. However, it is still very low. It may serve as a figure of merit to display the difference between a gravimetric excess isotherm and the corresponding blank-subtracted isotherm for an arbitrary sample.

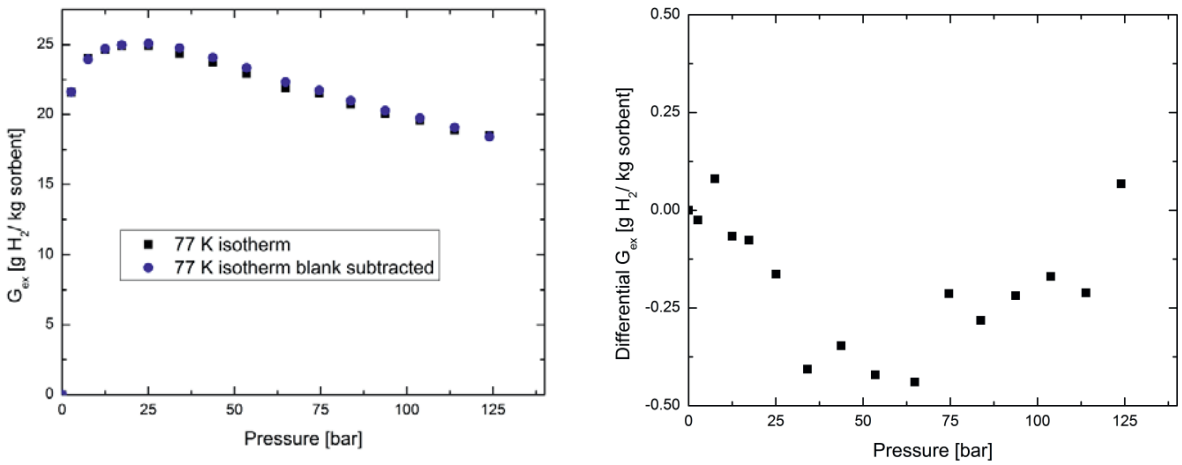

Figure 36 The difference between gravimetric excess isotherms and blank-subtracted gravimetric excess isotherm for sample HS;0B-20. *Left:* Isotherm and corresponding blank subtracted isotherm at 77 K. *Right:* Differential gravimetric adsorption between isotherm and their corresponding 77 K blank subtracted isotherm.

The gravimetric excess isotherm and corresponding blank-subtracted isotherms overlap one another. Subtracting the blank isotherm has little effect on the measured gravimetric excess, as long as the sample adsorbs a large amount relative to the blank. This holds true for all materials studied here at 77 K.

If a thermal bath is used to control the temperature, then the evaporation rate of the liquid, for example nitrogen, needs to be determined and f is not constant, it varies over time.

6.5 Validation of calibration

For validation purpose every six month the gravimetric excess adsorption at 77 K is recorded for one of the standard samples (HS;0B-20 or PVDC-414) and compared to previous measurements. This ensures all calibrated volumes are correctly determined. The H_2 adsorption performance of both standard adsorbent materials is roughly half that of high surface area carbon materials, making the measurement more sensitive to any occurring errors. Furthermore, material HS;0B-20 was send to the National Renewable Energy Laboratory (NREL) for external validation purpose.

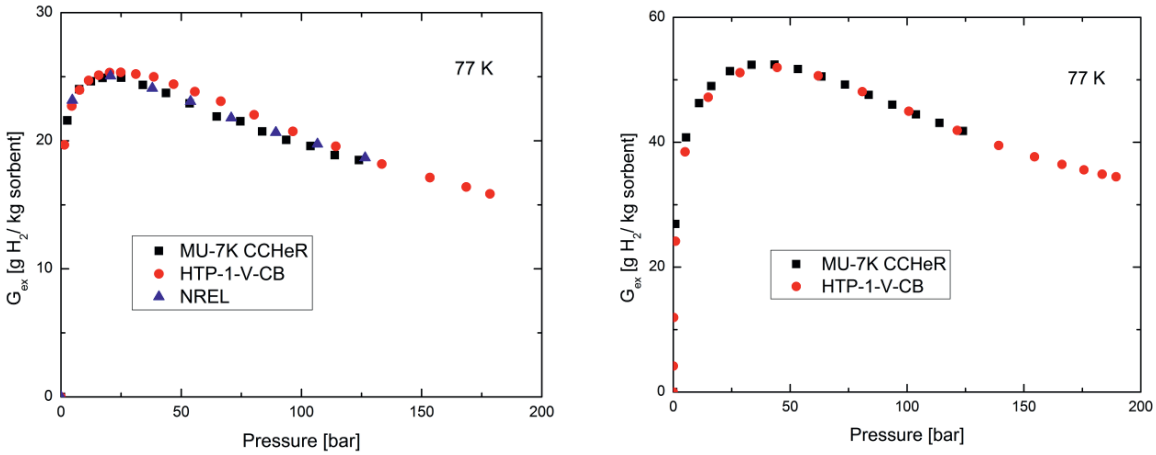

Figure 37 G_{ex} isotherms recorded on standard adsorbent material with 800 m^2/g (left) and 2300 m^2/g (right) specific surface area on different adsorption instruments.

The results of a typical validation are shown in Figure 37 and the agreement is within 2%. It does not only prove that the volumes are correct, it also validates the methods described earlier to obtain f and the dead space of the reactor. NREL measures the dead space before each experiment with He.

6.6 Error analysis

Excess adsorption calculations depend on a variety of variables such as temperatures, volumes of the dosing respectively reactor site, pressures and sample volume. Each of them contains an uncertainty which affects the calculation, and their effect can be calculated by the method of propagation of uncertainty. This requires calculating partial derivatives of G_{ex} with respect to all variables and the cumulative uncertainty is obtained via linearized partial derivate approximation according to equation 6.6.2. For simplicity, the gas density ρ_{gas} is expressed in terms of the compressibility factor Z according to

$$\rho_{\mathrm{gas}}(P,T) = \frac{P}{Z\mathrm{R}T} \tag{6.6.1}$$

where R equals the gas constant and, R and Z are not shown in equation 6.6.1.

$$\begin{aligned}\left|\Delta G_{\mathrm{ex},i}\right|^2 = {} & \left|\frac{\partial G_{\mathrm{ex}}}{\partial m_{\mathrm{s}}}\right|^2 \Delta m_{\mathrm{s}}^2 + \left|\frac{\partial G_{\mathrm{ex}}}{\partial V_{\mathrm{s}}}\right|^2 \Delta V_{\mathrm{s}}^2 + \left|\frac{\partial G_{\mathrm{ex}}}{\partial V_{\mathrm{r}}}\right|^2 \Delta V_{\mathrm{r}}^2 + \left|\frac{\partial G_{\mathrm{ex}}}{\partial V_{\mathrm{d}}}\right|^2 \Delta V_{\mathrm{d}}^2 + \left|\frac{\partial G_{ex}}{\partial T_d}\right|^2 \Delta T_d^2 \\ & + \left|\frac{\partial G_{\mathrm{ex}}}{\partial T_{\mathrm{s}}}\right|^2 \Delta T_s^2 + \left|\frac{\partial G_{\mathrm{ex}}}{\partial P_{\mathrm{I}i}}\right|^2 \Delta P_{\mathrm{I}i}^2 + \left|\frac{\partial G_{\mathrm{ex}}}{\partial P_{\mathrm{II}i}}\right|^2 \Delta P_{\mathrm{II}i}^2 + \left|\frac{\partial G_{\mathrm{ex}}}{\partial P_{\mathrm{III}i}}\right|^2 \Delta P_{\mathrm{III}i}^2 \\ & + \left|\frac{\partial G_{\mathrm{ex}}}{\partial f}\right|^2 \Delta f^2\end{aligned} \tag{6.6.2}$$

Partial derivatives of G_{ex} relative to all variables have been derived similar to equation 6.6.2 and the uncertainty in the measurement of each variable is represented by Δm_{s}, ΔV_{s}, ΔV_{r},…., Δf.

The uncertainties in system volumes V_{d} and V_{r} are estimated from the standard deviation governed from multiple hydrogen volume calibrations and are. In this study the sample volume was calculated from the dry sample mass m_{s} and a skeletal density ρ_{skel} of 2 g/cm^3 for carbon based material. The skeletal density was taken as an absolute value with no error, thus the error in V_{s} depends entirely on the mass measurement.

$$\Delta V_{\mathrm{s}} = \Delta m_{\mathrm{s}} * \rho_{\mathrm{skel}} \tag{6.6.3}$$

A precision balance from Mettler (PB503-s/Fact) with an error of 0.001 g was used to determine the adsrobent's dry mass, resulting in an error of 0.002 cm^3 for the sample volume.

The error in pressure is proportional to the accuracy of the pressure transducer picked for the experiment. The MU-7K CCHeR instrument is equipped with two pressure transducers; A high pressure transducer from General Electric (UNIK 5000) with an operating range from 0 to 200 bar, and a low pressure transducer from Sensotec (Super TJE Ultra) working from 0 to 2 bar, resulting in different uncertainties depending which one is used. The full-scale accuracy of the high pressure transducer is 0.04%, including non-linearity, hysteresis and repeatability and the low pressure one is rated to 0.05%, respectively. As a result $\Delta P_{\mathrm{I}i}$ = $\Delta P_{\mathrm{II}i}$ = $\Delta P_{\mathrm{III}i}$= 0.08 bar (high pressure) and $\Delta P_{\mathrm{I}i}$ = $\Delta P_{\mathrm{II}i}$ = ΔP_{IIIi}= 0.001 bar.

Another source of errors comes from the temperature of the dosing and reactor volume. The gas in the dosing volume is monitored with a high precision platinum resistance temperature detector (RTD) from Omega (Omega P-L-1/10-1/8-6-0-P-3) which has an accuracy of 0.04 K resulting in $\Delta T_{\mathrm{d}} = 0.04$ K. For each experiment, the reactor is placed into the copper enclosure of the CCR and insulated by a vacuum. The temperature of the copper block is controlled and monitored by calibrated silica diodes (DT-670, Lakeshore) and it is assumed T_{s} is equal to the temperature of the copper enclosure. The accuracy of silica diodes is not independent of the temperature, it increases at low temperature. Since the majority of adsorption experiments are carried out at 77 K, the error in ΔT_{s} was estimated by using the accuracy of the silica diode at that temperature, resulting in ΔT_{s} = 0.02 K.

In deriving the governing equation, the temperature of V_{d} and V_{r} are assumed to be different, leading to a factor f which describes how much volume of V_{r} is at a temperature different from the dosing volume. Unfortunately, there is not a direct way to estimate the error in

f since it is calculated by forcing the average excess adsorption of an empty isotherm to zero. To get an estimate of how large the error of f is, multiple blank isotherms at 77 K were recorded and their f values calculated. The error of f is then estimated by the standard deviation, leading to Δf = 0.5*10^{-4}.

Table 12 Uncertainties of parameters used in calculating G_{ex}

Sample mass (dry) $\Delta \boldsymbol{m_s}$ [g]:	0.001
Sample vol. $\Delta \boldsymbol{V_s}$ [cm^3]:	0.002
Sample reactor $\Delta \boldsymbol{V_r}$ [cm^3]:	0.009
Dosing vol. $\Delta \boldsymbol{V_d}$ [cm^3]:	0.03
Dosing temp. $\Delta \boldsymbol{T_d}$ [K]:	0.04
Sample temp. $\Delta \boldsymbol{T_s}$ [K]:	0.02 (at 77 K) 0.01 (at 20 K)
Pressure $\Delta \boldsymbol{P_{Ii}}$ [bar]:	0.08 (high pressure); 0.001 (low pressure)
Pressure $\Delta \boldsymbol{P_{IIi}}$ [bar]:	0.08 (high pressure); 0.001 (low pressure)
Pressure $\Delta \boldsymbol{P_{IIIi}}$ [bar]:	0.08 (high pressure); 0.001 (low pressure)
Fractional vol. $\Delta \boldsymbol{f}$:	0.5*10^{-4} estimated

6.7 Repeatability

One way of testing the quality of an instrument is its repeatability, meaning the differences in outcome if a measurement is repeated with all parameters held constant. Below is the absolute difference in G_{ex} for sample PVDC-410 for two consecutive isotherms. The sample was degassed in between each experiment at 200 ^{0}C for two hours.

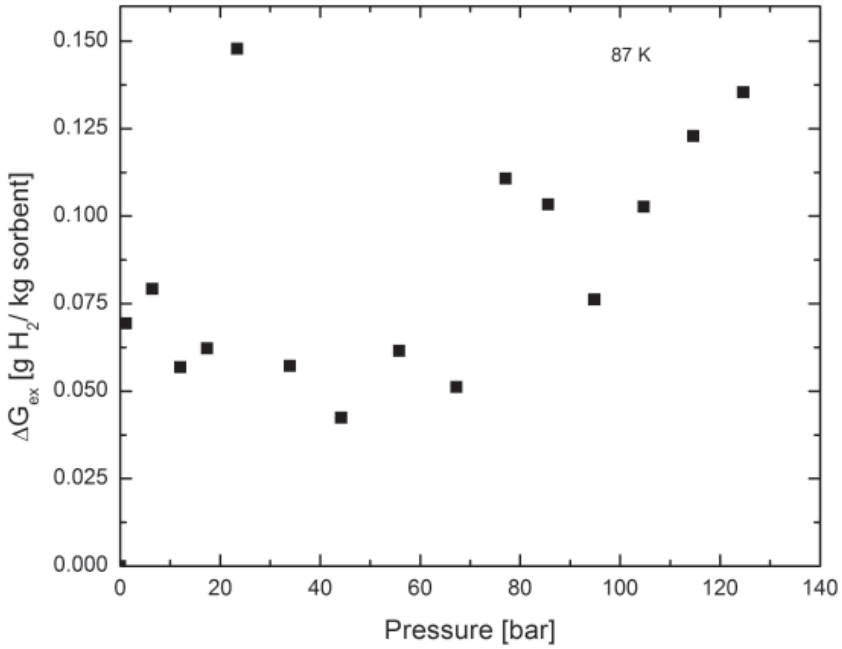

Figure 38 Repeatability of MU-7K CCHeR instrument.

The maximum deviation in G_{ex} reaches 0.15 g/kg at approximately 20 bar. It seems that at pressures >60 bar the differences in general are higher compared to low pressures. Comparisons of 77 K isotherms show a similar general trend. One reason for such an increased deviation at higher pressure could be due to small errors in fractional volume f. A slight difference in f affects the high pressure part of an isotherm, leaving the low pressure part unchanged. Therefore, small errors in f can lead to such behavior.

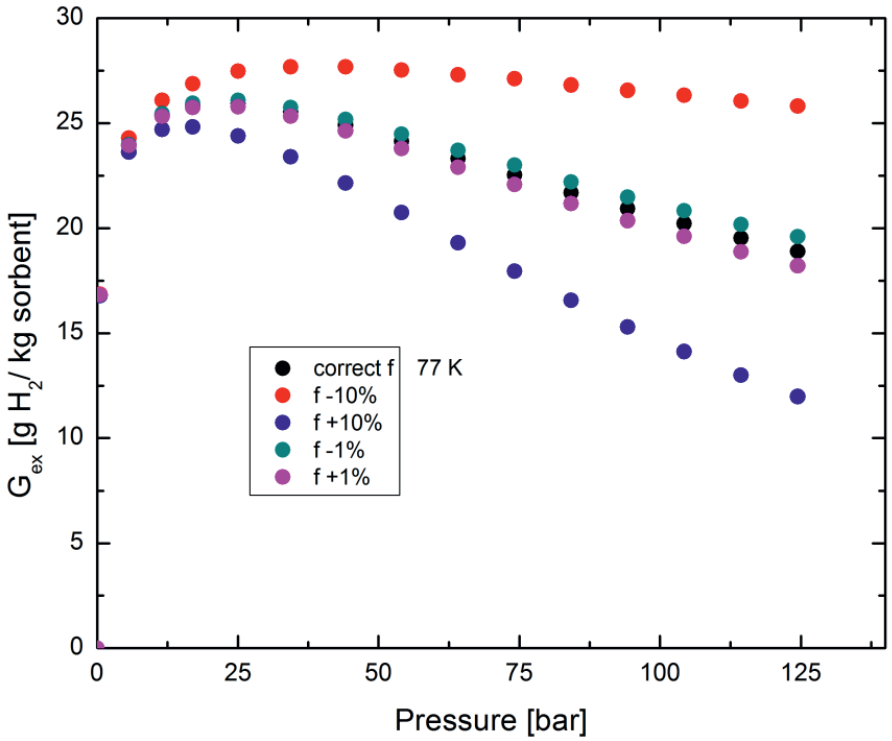

Figure 39 Graph shows G_{ex} at 77 K with a calibrated f (black), f plus/ minus 10 % (blue/ red), and f plus/ minus one % (magenta/ dark cyan).

An error as small as 1% can lead to deviations as large as 0.7 g/kg at 125 bar. Fractional volume can change slightly between each measurement, as the dosing volume temperature is only passively controlled via enclosure, and a small portion of the connecting tubing between the reactor and dosing site is exposed to room temperature. This capillary tube has an inner diameter of about 1 mm and is 50 cm long leading to a volume of $4*10^{-3}$ cm^3 without temperature control on the sample side. In calculating G_{ex} the temperature of this volume is assumed to be equal to the gas inside the dosing volume. This assumption can lead to errors if there is a difference in temperature between the enclosed volume and the room temperature.

Contributions from errors in temperature reading can be ruled out because RTDs measure temperature independent of the pressure in the system. Pressure transducers used in this system have decreasing uncertainties with increasing pressure, due to their design. Their uncertainty is measured in a percentage over the full scale (Strain Gauge Transducers). Furthermore, changes in

body volume can also be neglected because the system pressure is not high enough to expand the stainless steel tubes and connectors used.

Appendix

1. Sample preparation

The precursor material for synthetic carbons in this study is commercially available Saran© (copolymer of polyvinylidene chloride (PVDC) and polyvinyl chloride (PVC)) and a self-made PVDC homopolymer. The self-made PVDC was prepared via free radical homo polymerization from its monomer vinylidene chloride (VDC, Sigma Aldrich) in benzene or cyclohexane according to the following reaction scheme below.

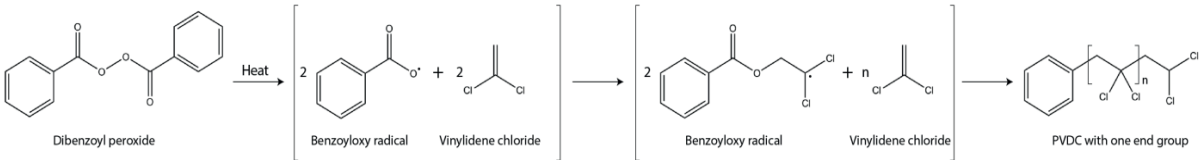

The commercially available monomer has a small amount of 4-Methoxylphenol (MEHQ) as an inhibitor to prevent bulk polymerization during shipment or storage. The inhibitor was removed prior to polymerization to preserve yield by washing the VDC twice with 10% sodium hydroxide (NaOH) solution and subsequent distillation of the product at 60 °C under argon. Afterwards 262.7 mmol VDC was dissolved in 28.4 mL cyclohexane (oxygen free) and placed into an argon purged flask. Dibenzoyl peroxide (DBP) (3 mmol) dissolved in cyclohexane was added to initiate the radical reaction [39]. The mixture was heated at 50°C for 64 hours, forming a white solid product. Afterwards the product was dried overnight in a vacuum oven at room temperature to remove any remaining solvent or monomer. This procedure gave a 77% yield.

After initiating the reaction by heating the mixture, benzoyloxy radicals successively react with the allyl group of the monomer, forming a radical species of the monomer. The radical monomer propagates by adding monomer molecules, forming long polymer chains. Termination can occur by combining two chains or disproportionation of two radicals. In these cases the radical starter ends up in one or both end group positions.

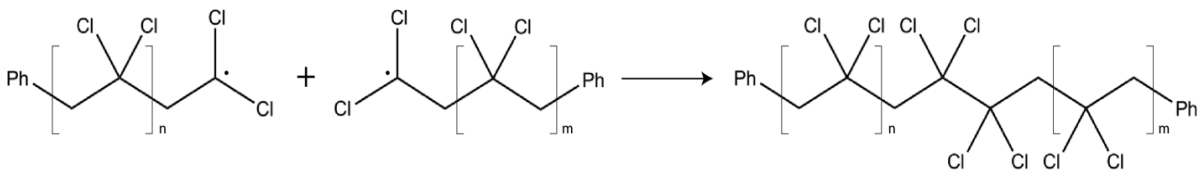

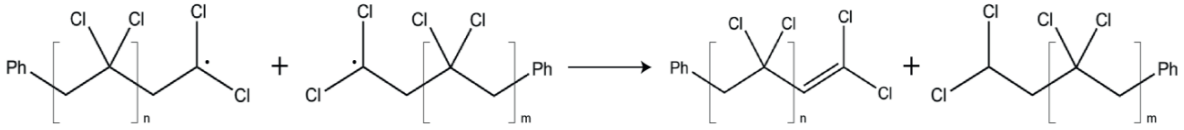

Another stopping mechanism is via chain transfer, wherein one hydrogen atom combines with the radical species terminating chain growth.

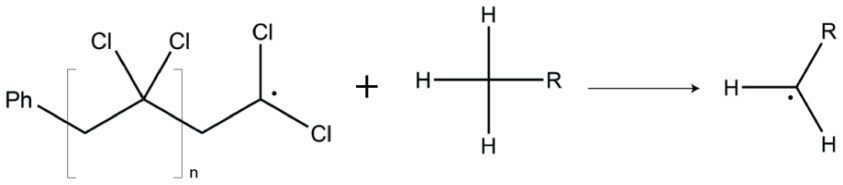

2. Pyrolysis mechanism

Upon pyrolysis, the PVDC homopolymer forms various aromatic structures. DBP was chosen as a radical initiator, as it contains an aromatic ring, which would easily embed into the post-pyrolysis structure of PVDC. The two oxygen atoms of DBP will form carbon dioxide or carbon monoxide during heat treatment, creating surface defects, and therefore potentially strong hydrogen adsorption sites.

In the absence of oxygen, PVDC begins to decompose at 140 ^{o}C with the rate of decomposition increasing between 150 ^{o}C and 200 ^{o}C [40,41]. During heating, chlorine combines in a zipper-type reaction with its neighboring hydrogen atom, forming gaseous HCl and resulting in the formation of polyacetylene structures on the polymer's carbon backbone [40,41].

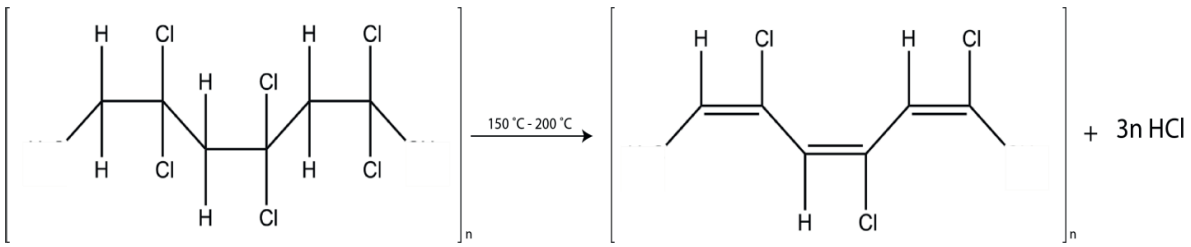

In the next step two polyene chains combine, forming cyclic rings with a mechanism similar to the Diels Alder reaction [40]. An electron-rich (diene) structure reacts with an electron-deficient (dienophile) to form a cyclohexene system (Scheme 2), yielding a shimmering brown product [40]. The evolution of HCl decreases over time due to a lack of adjacent chlorine atoms. At this point most of the chlorine is consumed and the distance between individual chlorine atoms is more than one carbon to carbon distance apart. Once this occurs, it is believed that the chlorines can change their position on the carbon chain due to high temperature and conducive circumstances until they find a favorable site to recombine with hydrogen, and continue to form HCl gas [40]. This explains some of the weight loss in the thermogravimetric analysis curve at temperatures above 400 ^{0}C observed by Bin Xu et al. [42]. Typically a reduction of 75% in sample mass can be observed. The formation of carbon monoxide and carbon dioxide from chemically bound oxygen also contributes to the mentioned weight loss.

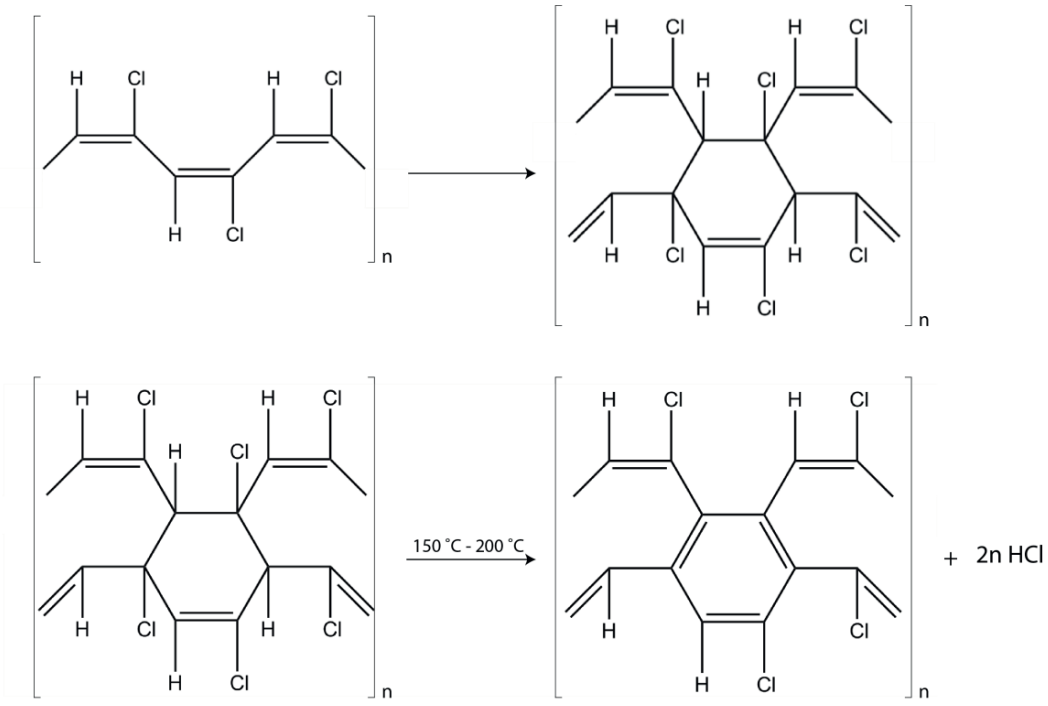

3. Material Properties

Material properties such as total surface area, porosity, total pore volume, and pore size distribution have an influence on the material`s performance. These properties are mainly influenced by the chemical composition of the polymer and the pyrolysis process.

The chemical composition of polymers can be altered by using different types and mixtures of monomers during polymerization. For example Saran© is made by polymerization of a mixture of vinylidene chloride and vinyl chloride. This results in a copolymer which contains different arrangements of PVDC and PVC depending on the monomer ratio and polymerization process. The polymerization process itself also has an influence on the polymer. For example, the amount of initiator used during radical polymerization affects the mean molecular weight of the polymer. The weight decreases with increasing quantities of radical initiator. The heating rate during pyrolysis is another factor that has an effect on the material. HCl is released rapidly with increased heating rate, forming bubbles similar to foam.

4. PVDC composition

As previously mentioned, two different sorts of PVDC-based polymer were used during this study: the commercially available copolymer Saran©, consisting of PVDC and PVC, and the homopolymer PVDC. The PVDC was fabricated by radical polymerization in our lab, which guaranteed full control of the polymer`s composition. Saran© (Figure 4) has an uneven chloride to hydrogen ratio in its idealized unit cell compared to pure PVDC (Figure 5). This ratio affects the porosity, pore volume, and surface area.

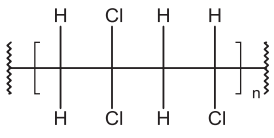

Figure 1 Idealized unit cell Saran©

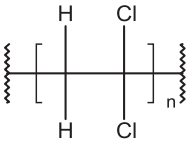

Figure 2 Idealized unit cell PVDC

Two samples, one from the homopolymer (PVDC-412) and a Saran© based sample (PVDC-414), were heat treated under the same conditions. First, the temperature was increased from 25 °C to 170 °C at a rate of 0.5 $\frac{^0C}{min.}$ and held at 170 °C for two hours. Then the temperature was increased to 700 °C at 2 $\frac{^0C}{min.}$ and held there for two hours. Slow heating ensures that the volatile gas has enough time to diffuse through the polymer giving a uniform sample composition without visible cracks and creating a uniform surface. But fast heating results in “foaming” and a non-uniform sample with visible holes and a rough surface. The complete procedure was carried

out under a flow of N_2 to make sure no carbon reacted with oxygen. In the final step, both samples where ground into a fine powder to ensure sample homogeneity. The sample properties were measured using an automated gas adsorption instrument from Quantachrome (Autosorb-1). The table below lists adsorption properties governed by subcritical nitrogen isotherms.

	BET surface area $\left[\frac{\mathrm{m}^2}{\mathrm{g}}\right]$	BET C value	Total pore volume $\left[\frac{\mathrm{cm}^3}{\mathrm{g}}\right]$ (N_2 @ 0.995 $\frac{P}{P_0}$)	Pore volume $\left[\frac{\mathrm{cm}^3}{\mathrm{g}}\right]$ (Pore width < 0.79 nm; NLDFT)	Porosity
PVDC-412	1140	2024	0.71	0.32	0.59
PVDC-414	810	2344	0.47	0.23	0.49

Table 13 Material property of Saran and PVDC based sample

The BET specific surface areas (seven point) of the homopolymer (PVDC-412) and its copolymer (PVDC-414), evaluated over the pressure range 0.008-0.03 $\frac{P}{P_0}$, are about 1140 $\frac{m^2}{g}$ and 810 $\frac{m^2}{g}$, respectively. Saran© has a 300 $\frac{m^2}{g}$ lower specific surface area, and its total pore volume, measured at 0.995 $\frac{P}{P_0}$, is about half that of the pure polymer. Note that total pore volume calculated at 0.995 $\frac{P}{P_0}$ includes micro and macro pore space, and it is therefore a good measurement for the entire pore space. Porosity and sub-nanometer pore volume (pore width < 0.79 nm) are also affected by the chemical composition. The above results seem to indicate pure PVDC produces a more porous sample compared to its copolymer.

It is possible that Saran© is not able to form as much hydrochloric acid during pyrolysis compared to the homopolymer, as it starts out with one fewer chlorine atom, and therefore forms less HCl. Scheme three shows the pyrolysis process for Saran©, which is similar to the one described earlier.

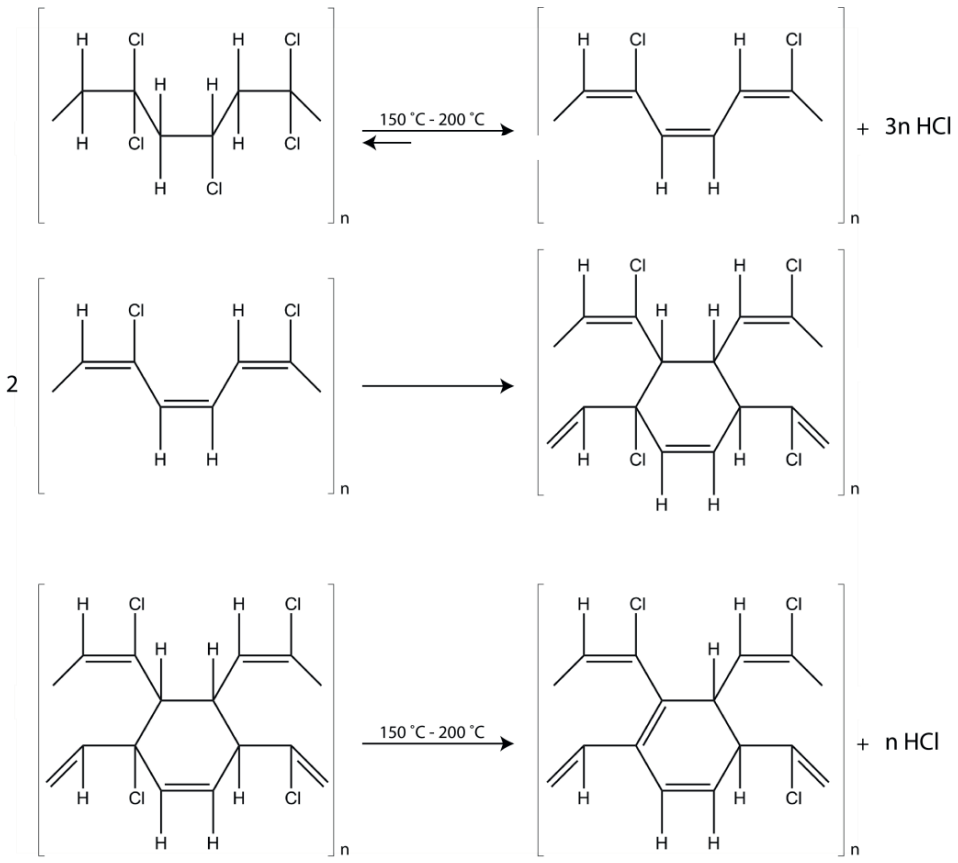

Scheme 1 Chemical reaction of Saran© during heating

The first two steps are identical with the ones in scheme one and two; however, in the last step one equivalent of hydrochloric acid is released, one fewer than the homopolymer. The pure PVDC's idealized unit cell has chlorine instead of hydrogen bound to the 4th carbon (from left), which can form another HCl molecule and therefore is able to create more pores.

Unfortunately copolymers are not very well ordered, and the idealized picture of repeating unit cells is oversimplified. Depending on the monomer ratio and how the polymerization was carried out it is possible to obtain alternating copolymers (e.g. $(A\text{-}B\text{-}A\text{-}B\text{-}A)_n$), periodic copolymers (e.g. $(A\text{-}B\text{-}A\text{-}A\text{-}A\text{-}B\text{-}B)_n$), or Block copolymers (e.g. $(A\text{-}A\text{-}A\text{-}B\text{-}B\text{-}B\text{-}B\text{-}A\text{-}A\text{-}A)_n$). Therefore, Saran can still contain some regions which consist of pure PVDC. But it is generally rare to find such regions, as Saran© does not have a stoichiometric ratio of hydrogen and chlorine, meaning some chlorine atoms are not involved in pore construction.

REFERENCES

[1] J. Kopyscinski, T. J. Schildhauer, and S. M. a Biollaz, Fuel **89**, 1763 (2010).

[2] L. Schlapbach and A. Züttel, Nature **414**, 353 (2001).

[3] TOTE, TOTE launches world's first LNG powered containership, http://toteinc.com/tote-launches-wolrds-first-lng-powered-containership/,(2015).

[4] Toyota, Hydrogen Tank FCV, www.toyota-global.com/innovation/enviromental_technology/fuelcell_vehicle/,(2015).

[5] N. Stock and S. Biswas, Chem. Rev. **112**, 933 (2012).

[6] Y.-R. Lee, J. Kim, and W.-S. Ahn, Korean J. Chem. Eng. **30**, 1667 (2013).

[7] J. Romanos, M. Beckner, T. Rash, L. Firlej, B. Kuchta, P. Yu, G. Suppes, C. Wexler, and P. Pfeifer, Nanotechnology **23**, 015401 (2012).

[8] J. Burress, M. Kraus, M. Beckner, R. Cepel, G. Suppes, C. Wexler, and P. Pfeifer, Nanotechnology **20**, 204026 (2009).

[9] J. E. Jones, Proc. R. Soc. A Math. Phys. Eng. Sci. **106**, 441 (1924).

[10] H. Everett and J. C. Powl, (1975).

[11] T. Hill, *An Introduction to Statistical Thermodynamics* (Dover Publications, 1960).

[12] P. G. Menon, Chem. Rev. **68**, 277 (1968).

[13] E. Poirier and A. Dailly, Langmuir **25**, 12169 (2009).

[14] E. Poirier and A. Dailly, J. Phys. Chem. C **112**, 13047 (2008).

[15] G. Aranovich and M. Donohue, J. Colloid Interface Sci. **194**, 392 (1997).

[16] M. Beckner, (2012).

[17] Y. Ferro, F. Marinelli, A. Allouche, and C. Brosset, J. Chem. Phys. **118**, 5650 (2003).

[18] L. Firlej, S. Roszak, B. Kuchta, P. Pfeifer, and C. Wexler, J. Chem. Phys. **131**, 164702 (2009).

[19] J. Moellmer, A. Moeller, F. Dreisbach, R. Glaeser, and R. Staudt, Microporous Mesoporous Mater. **138**, 140 (2011).

[20] J. Li and E. Wu, J. Supercrit. Fluids **49**, 196 (2009).

[21] P. G. Menon, Adsorption of Nitrogen and Carbon Monoxide on Alumina up to 3000 Atmospheres Pressure, Delft, 1961.

[22] F. Rouquerol, J. Rouquerol, and K. Sing, *Adsorption by Powders and Porous Solids* (Elsevier, 1999).

[23] S. Brunauer, P. H. Emmett, and E. Teller, J. Am. Chem. Soc. **60**, 309 (1938).

[24] E. Solomon, AIChE J. **1**, 272 (1955).

[25] C. M. Brown, Y. Liu, T. Yildirim, V. K. Peterson, and C. J. Kepert, Nanotechnology **20**, 204025 (2009).

[26] C. Prestipino, L. Regli, J. G. Vitillo, F. Bonino, A. Damin, C. Lamberti, A. Zecchina, P. L. Solari, K. O. Kongshaug, and S. Bordiga, Chem. Mater. **18**, 1337 (2006).

[27] J. Purewal, D. Liu, A. Sudik, M. Veenstra, J. Yang, S. Maurer, U. Müller, and D. J. Siegel, 1 (n.d.).

[28] A. McClellan and H. Harnsberger, J. Colloid Interface Sci. **23**, 577 (1967).

[29] Y.-J. Kim, Y. Masutzawa, S. Ozaki, M. Endo, and M. S. Dresselhaus, J. Electrochem. Soc. **151**, E199 (2004).

[30] K. Kaneko, C. Ishii, M. Ruike, and H. kuwabara, Carbon N. Y. **30**, 1075 (1992).

[31] L. E. C. De Torre and E. J. Bottani, **7463**, 5399 (1996).

[32] B. Streppel and M. Hirscher, Phys. Chem. Chem. Phys. **13**, 3220 (2011).

[33] H. W. Melville, *The Interaction of Gases with Solids* (Pergamon Press, 1935).

[34] A. Sieverts, Zeitschrift F{ü}r Met. **21**, 37 (1929).

[35] D. P. Broom, Int. J. Hydrogen Energy **32**, 4871 (2007).

[36] E. W. Washburn and E. N. Bunting, J. Am. Ceram. Soc. **5**, 527 (1922).

[37] F. A. P. MAGGS, P. H. SCHWABE, and J. H. WILLIAMS, Nature **186**, 956 (1960).

[38] A. V Neimark and P. I. Ravikovitch, **i**, 5148 (1997).

[39] D. Braun, H. Cherdron, M. Rehahn, H. Ritter, and B. Voit, *Polymer Synthesis: Theory and Practice: Fundamentals, Methods, Experiments* (Springer Science & Business Media, 2012).

[40] J. R. Dacey and R. G. Barradas, Can. J. Chem. **41**, 180 (1963).

[41] R. Bohme and R. Wessling, J. Appl. Polym. Sci. **16**, 1761 (1972).

[42] B. Xu, F. Wu, S. Chen, Z. Zhou, G. Cao, and Y. Yang, Electrochim. Acta **54**, 2185 (2009).

VITA

Elmar Dohnke was born on January 16, 1982 in Würzburg, Germany. He received his Diploma in applied physics from University of applied science Coburg in 2010. In 2014 he received a MS in Physics from the University of Missouri. He received a PhD in Physics from the University of Missouri in 2015 under the advisement of Peter Pfeifer.